Creep-Fatigue Damage Investigation and Modeling of Alloy 617 at High Temperatures

by

Fraaz Tahir

A Dissertation Presented in Partial Fulfillment
of the Requirements for the Degree
Doctor of Philosophy

Approved April 2017 by the
Graduate Supervisory Committee:

Yongming Liu, Chair
Hanqing Jiang
Jay Oswald
Jagannathan Rajagopalan
Yang Jiao

ARIZONA STATE UNIVERSITY

May 2017

ABSTRACT

The Very High Temperature Reactor (VHTR) is one of six conceptual designs proposed for Generation IV nuclear reactors. Alloy 617, a solid solution strengthened Ni-base superalloy, is currently the primary candidate material for the tubing of the Intermediate Heat Exchanger (IHX) in the VHTR design. Steady-state operation of the nuclear power plant at elevated temperatures leads to creep deformation, whereas loading transients including startup and shutdown generate fatigue. A detailed understanding of the creep-fatigue interaction in Alloy 617 is necessary before it can be considered as a material for nuclear construction in ASME Boiler and Pressure Vessel Code. Current design codes for components undergoing creep-fatigue interaction at elevated temperatures require creep-fatigue testing data covering the entire range from fatigue-dominant to creep-dominant loading. Classical strain-controlled tests, which produce stress relaxation during the hold period, show a saturation in cycle life with increasing hold periods due to the rapid stress-relaxation of Alloy 617 at high temperatures. Therefore, applying longer hold time in these tests cannot generate creep-dominated failure. In this study, uniaxial isothermal creep-fatigue tests with non-traditional loading waveforms were designed and performed at 850 and 950°C, with an objective of generating test data in the creep-dominant regime. The new loading waveforms are hybrid strain-controlled and force-controlled testing which avoid stress relaxation during the creep hold. The experimental data showed varying proportions of creep and fatigue damage, and provided evidence for the inadequacy of the widely-used time fraction rule for estimating creep damage under creep-fatigue conditions. Micro-scale damage features in failed test specimens, such as fatigue cracks and creep voids, were quantified using a Scanning Electron Microscope

(SEM) to find a correlation between creep and fatigue damage. Quantitative statistical imaging analysis showed that the microstructural damage features (cracks and voids) are correlated with a new mechanical driving force parameter. The results from this image-based damage analysis were used to develop a phenomenological life-prediction methodology called the effective time fraction approach. Finally, the constitutive creep-fatigue response of the material at 950°C was modeled using a unified viscoplastic model coupled with a damage accumulation model. The simulation results were used to validate an energy-based constitutive life-prediction model, as a mechanistic model for potential component and structure level creep-fatigue analysis.

ACKNOWLEDGMENTS

I would like to express my sincere gratitude to my advisor, Dr Yongming Liu for his guidance and unwavering support throughout the duration of my studies. I would like to thank him for his mentorship and valuable insights which helped me achieve my research objectives. I would also like to thank the members of my Supervisory Committee, Prof. Hanqing Jiang, Prof. Jagannathan Rajagopalan, Prof. Jay Oswald, and Prof. Yang Jiao for volunteering their time to provide advice regarding my research.

This work was sponsored by the U.S. Department of Energy under the Nuclear Energy University Programs (NEUP) initiative (DE-NE0000675). I gratefully acknowledge Richard Wright (Idaho National Lab) for his advice on testing methods and Sam Sham (Argonne National Lab) for his valuable input on model development and prediction methodology.

I am grateful to my fellow group members, current and former, for their willingness to help and their strong work ethic which motivated me in my own research. Special thanks to Hailong Chen for being a sounding board for my research ideas and for providing insightful suggestions and to Sonam Dahire for helping me in the material characterization part of this research.

TABLE OF CONTENTS

Page

CHAPTER Page

CHAPTER Page

LIST OF TABLES

Table Page

LIST OF FIGURES

Figure Page

Figure Page

Figure Page

Figure Page

Figure Page

1. BACKGROUND AND MOTIVATION

Creep-fatigue is an important damage mechanism in high-temperature systems that undergo cyclic thermal stresses interspersed with periods of constant load. Examples of such systems include gas turbines, heat exchangers, and microelectronics packaging [1,2]. Recent interest in creep-fatigue interaction in superalloys is driven by the need to evaluate structural materials for future nuclear power plants. The Very High Temperature Reactor (VHTR) is one of six conceptual designs proposed for Generation IV nuclear reactors. The VHTR is a gas-cooled reactor with helium as the primary coolant. The coolant is expected to reach temperatures up to 950°C at the reactor outlet, before passing through an Intermediate Heat Exchanger (IHX) - which provides process heat for electricity and hydrogen production [3,4]. Steady-state operation of the plant at elevated temperatures leads to creep deformation, whereas loading transients including startup and shutdown generate fatigue [5,6]. Hence, creep-fatigue interaction is expected to be a major damage mechanism for structural materials in the IHX. Alloy 617 - a solid-solution strengthened nickel-base superalloy - is the leading candidate material for IHX tubing due to its thermal stability, creep strength, and oxidation resistance at high temperatures [5,7,8]. A detailed understanding of the creep-fatigue interaction in Alloy 617 is necessary before it can be considered as a material for nuclear construction in ASME Boiler and Pressure Vessel Code, Section III, Subsection NH [9].

A majority of current creep-fatigue life prediction methods are based on time fraction rule (TFR), ductility exhaustion (DE), or strain-range partitioning (SRP) [10]. Nuclear component design codes, namely ASME BPVC, Section III, Subsection NH[9], RCC-MR [11], and R5 [12], suggest linear summation of creep and fatigue damage

fractions to predict failure. ASME and RCC-MR require a time fraction – based on TFR – for calculating creep damage, whereas R5 requires a strain fraction calculation based on DE. One limitation of the DE approach is that the value of creep fraction can exceed unity for some materials, leading to highly conservative predictions [10,13,14]. Takahashi [13] proposed a modified ductility exhaustion method to alleviate this limitation. The SRP method works well when enough test data is available to partition the total strain range. Hoffelner [15] improved life prediction in SRP by modifying the creep strain partition.

The time fraction rule can be used to predict creep-fatigue life with the help of the following relation:

$$\sum_{i}\left(\frac{n}{N_f}\right)_i + \sum_{j}\left(\frac{\sum t_h}{T_r}\right)_j \leq D \qquad (1)$$

where n is the cycles to failure in creep-fatigue, N_f is the cycles to failure in pure fatigue for the given strain range, t_h is the hold time in each cycle, T_r is the time to rupture in pure creep for a given stress and temperature and D is the allowable combined damage fraction. In this study, N_f was found from a fatigue strain-life curve and T_r was calculated from a Larson-Miller plot. The first term in Eq. (1) is a cycle fraction representing fatigue damage and the second term is a time fraction representing creep damage. The damage fractions for Alloy 617 at 950°C are expected to follow a bilinear curve on a creep-fatigue interaction diagram [6] as is typical for steels (see Fig. 1.1).

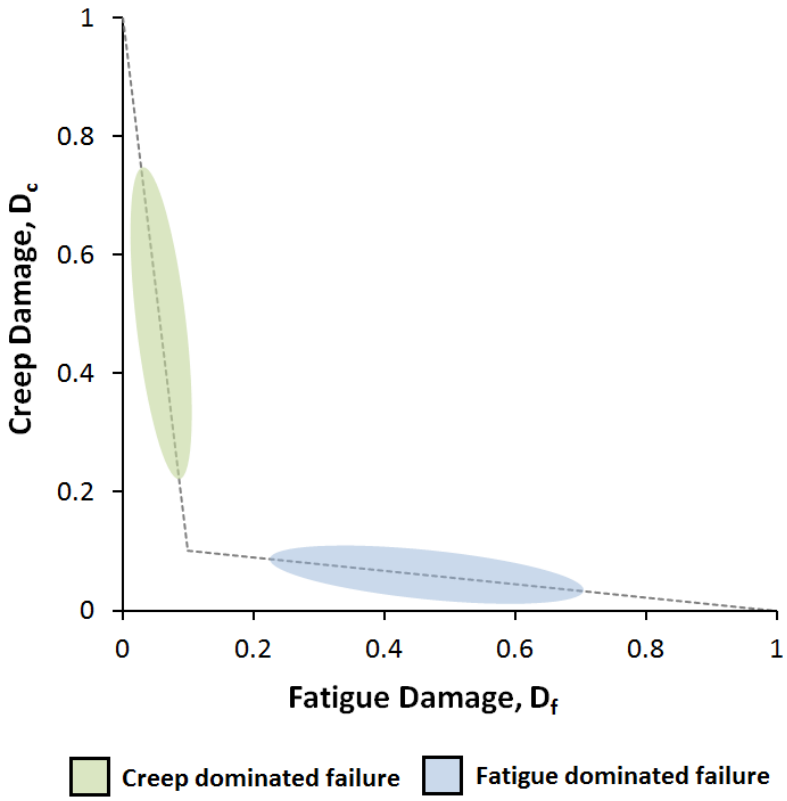

Fig. 1.1 – Creep-fatigue interaction diagram highlighting the creep-dominant and fatigue-dominant regimes.

Traditional strain-controlled tests cannot produce creep-dominated failure due to the rapid stress-relaxation of Alloy 617 at high temperatures. Therefore, force-controlled loading waveform must be investigated as a means for generating greater creep damage. Additionally, existing creep-fatigue tests for Alloy 617 at 950˚C, do not show a trend when plotted on an interaction diagram. This is due to unrealistic values of creep damage fraction resulting from the time fraction rule. Exploration of loading waveforms with force-controlled hold periods can directly induce creep damage and therefore act as validation check for the widely used time fraction rule.

The goals of this study are:

1. To propose novel test procedures to generate creep-dominated creep-fatigue interaction with the introduction of force-controlled tensile hold periods.
2. To qualitatively and quantitatively distinguish between creep and fatigue dominated damage in failed creep-fatigue test specimens using Scanning Electron Microscopy (SEM), Electron Backscatter Diffraction (EBSD), Energy Dispersive Spectroscopy (EDS) and optical profilometry.
3. To propose a life prediction methodology based on the findings from micro-scale damage analysis.
4. To obtain an improved life-prediction by modeling the constitutive response of the material under creep-fatigue cycling using a unified viscoplastic model with damage.

2. NEW CREEP-FATIGUE EXPERIMENTAL TESTING METHOD

2.1 INTRODUCTION

Several experimental studies have been conducted in the past to investigate the creep-fatigue behavior of Alloy 617 at elevated temperatures. Rao et al.[16] conducted strain-controlled creep-fatigue tests on Alloy 617 at 950°C in a helium environment to determine the effect of strain rate, hold time, and hold condition (i.e., tension or compression hold) on the creep-fatigue lives. They concluded that introducing a hold period at peak strain reduced the cycle life and that a tension hold was more damaging than either a compression hold or a combination of tension and compression hold. They also observed that tests with short tensile hold periods produced transgranular cracks whereas tests with tensile hold periods longer than 10 min produced intergranular cracks. Fatigue dominated failures are typically accompanied by transgranular cracking whereas creep dominated failures are accompanied by intergranular cracking and creep cavitation [17]. However, Cabet et al.[17] carried out strain-controlled creep-fatigue tests on Alloy 617 at 950°C in air and observed intergranular cracking but no grain boundary cavitation, even with hold times as long as 1800s with a strain range of 0.6%. This suggests that generating creep-dominant creep-fatigue testing data will be very difficult using purely strain-controlled testing, which is due to the very rapid stress relaxation for materials at high temperatures. For component design against creep-fatigue, the classical strain-based testing method will be insufficient to provide enough data to construct the damage diagram (see Fig. 1.1).

The ASTM standard for creep-fatigue testing E2714-13 provides examples of strain-controlled loading profile with a hold at peak strain and force-controlled loading profile with a hold at peak stress. For Alloy 617, it is known that tensile hold periods are more damaging than compressive hold periods [16,18]. Moreover, for a purely strain-controlled loading profile, the stress during the hold period becomes steady after the initial rapid stress relaxation. Therefore, after a certain threshold value, a longer hold time does not produce more creep damage. To solve this problem, Fournier et al. [19] conducted tests with a force-controlled hold period on 9Cr-1Mo martensitic steel at 550°C. They observed that fatigue life was reduced but the creep damage remained low. Simpson et al. [6] suggested that, for Alloy 617 at 950°C, creep-dominant damage may be produced by a loading profile similar to one used by Fournier et al. [19], but there is no experimental evidence to support this hypothesis. In addition, TFR does not fully account for the dependence of life on the type of loading waveform so it can be inaccurate when applied to unconventional creep-fatigue loading [10,11]. Thus, any new testing method for generating creep fatigue data must be carefully investigated with respect to the TFR methodology.

Based on the above brief review and discussion, the objective of this study is to experimentally explore the possible creep-fatigue testing procedures for generating creep-dominant failure, which will aid in the construction of a damage interaction diagram for creep-fatigue design. Several non-traditional creep-fatigue loading profiles, such as stress-controlled, hybrid control with specified hold time, hybrid control with specified hold strain, and cyclic ratcheting are investigated and compared for their suitability for producing creep-dominant damage.

2.2 EXPERIMENTAL PROCEDURE

An MTS servo-hydraulic load frame equipped with a high temperature furnace was used to conduct the creep-fatigue tests. The specimens of Alloy 617 were standard round-section specimens with tangentially blending fillets and button-head ends with a gage length of 20mm and gage diameter of 7.5mm. The long axis of the specimen was parallel to the rolling direction. All tests were performed at constant temperature of 950°C using a furnace that consisted of three pairs of silicon-carbide heating elements. Temperature control was achieved with K-type thermocouples wrapped on to the specimen using silica wick. Four thermocouples were used: two on the grips and two the specimen shoulders. The temperature difference along the gage length was controlled to be less than 10°C for all tests. Strain measurement was achieved by an air-cooled high-temperature extensometer with ceramic extension rods which maintained contact with the gage length of the specimen. The maximum range for the extensometer was 24% strain so for tests with larger total strain - e.g. due to ratcheting – the extensometer had to be reset within the test. A strain rate of 1×10^{-3}/s was used for all strain-controlled ramps. A hand pump was used to apply a pressure of 200 psi to the grips. It was observed that applying a higher pressure caused damage to the grips and specimen at 950°C. The experimental setup is shown in Fig. 2.1.

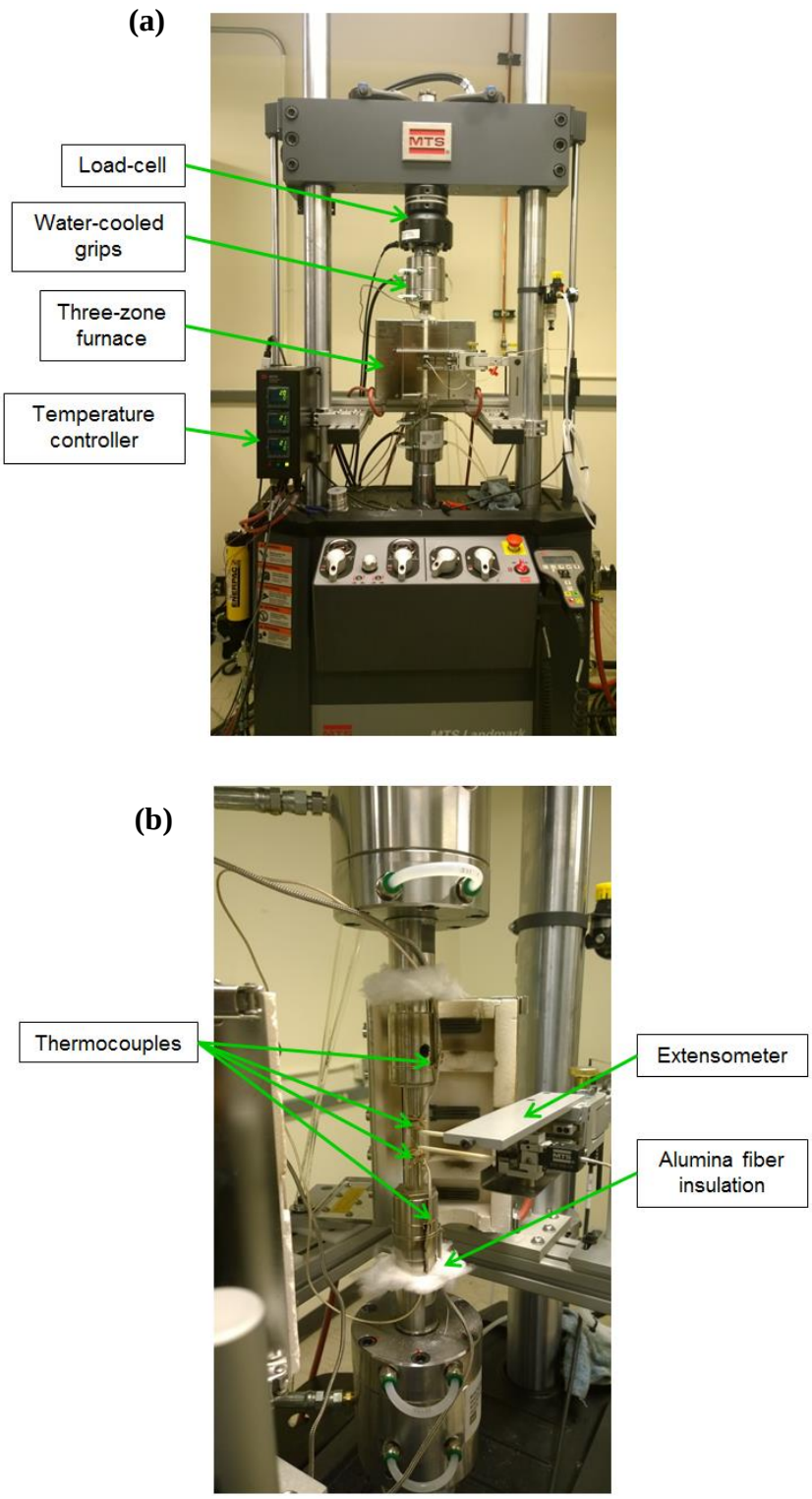

Fig. 2.1 – (a) Load frame with high-temperature system; (b) Test specimen installed between grips.

Traditional strain-controlled fatigue stress-relaxation testing of Alloy 617 at 950°C cannot populate the creep-dominant part of the creep-fatigue interaction diagram [6]. Hence, loading waveforms with force-controlled hold must be applied to generate creep-dominant damage. New loading waveforms were implemented to study creep-fatigue interaction in the creep-dominant regime. These waveforms can be classified as: (i) purely force-controlled; (ii) hybrid-control with stress hold at peak strain; (iii) hybrid-control with an intermediate stress hold and (iv) hybrid-control with ratcheting and intermediate stress hold. The term 'hybrid' here, refers to a combination of stress and strain control. The end-of-test criterion for the force-controlled tests was complete rupture whereas for all other tests it was a 50% drop in maximum tensile stress. In these tests, creep strain $\varepsilon_{c,}$ is defined as the strain accumulated during the hold period [19]; fatigue strain range, $\Delta\varepsilon_f$, is defined as the difference between the total strain range, $\Delta\varepsilon_t$, and creep strain. To prevent large data sets, cycle data was collected every 5 or 10 cycles, depending on the expected cycle life of the given test. The loading profiles discussed here were not available in the standard MTS fatigue database, custom loading profiles were programmed in MTS Multipurpose Elite software. Hybrid control requires a switch from a strain-controlled ramp to a force-controlled hold for each cycle. This was achieved in the software by running a force limit detector in parallel with the strain ramp command. The following sections will explain each of the tests in detail.

2.2.1 Purely Force-Controlled Test

The idea behind using force-control is to replace the stress-relaxation part of the traditional strain-controlled loading waveform with creep deformation induced by a

force-controlled hold. The entire test was performed in force-control. Loading and unloading ramps were executed at 1000 N/s, whereas the peak stress was held constant for a fixed time of 30s per cycle as shown in Fig. 2.1(a). The strain amplitude increased with cycles due to softening. The mean strain also increased indicating ratcheting. Fig. 2.1(b) shows the ratcheting behavior between first, mid and last cycles. The ratcheting, in this case, is a consequence of completely reversing the force instead of the strain. Three tests were conducted with stress amplitudes of 40, 55 and 70 MPa respectively. In all three tests, the creep damage fraction, D_c, was greater than unity and fatigue damage fraction, D_f, was close to zero. These fractions suggest highly creep-dominant damage and therefore, an absence of creep-fatigue interaction. It was observed that applying a waveform with higher stress amplitude does not lead to an increase in the fatigue fraction. Applying shorter hold periods may cause a reduction in D_c and an increase in D_f. However, using hold periods less than 30s to produce creep-dominant damage is not recommended because the creep damage incurred during the hold period may be less than the creep damage during the loading and unloading parts of the cycle.

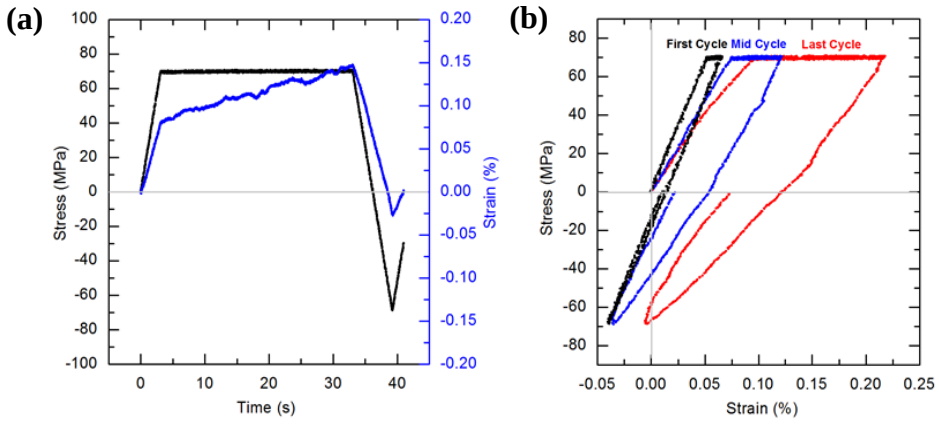

Fig. 2.2 – (a) Applied stress profile and corresponding strain response for one cycle; (b) Stress-strain curves for first, mid and last cycle showing ratcheting. The initial strain is changed to zero to compare the cycles

2.2.2 Hybrid-Control with Stress Hold at Peak Strain

A hybrid-control test, similar to the one conducted by Fournier et al [19] for steels, was investigated for Alloy 617. For the test shown in Fig. 2.3(a), strain is ramped at a rate of 1×10^{-3}/s to 0.45% first. Following this, the control is switched from strain to force and the corresponding force is held constant until the strain reaches 0.75%. Next, strain is reversed to -0.45% in strain control and then this cycle is repeated. In this loading waveform, complete reversal of strain prevents cyclic ratcheting. The peak stress is held constant up to a fixed strain level, the hold time increases with cycles due to softening as shown in Fig. 2.3(b). The sudden increase in stress during the compressive part of the last cycle, seen in Fig. 2.3(a), indicates crack closure. The holding stress in this type of loading waveform can be larger than yield stress. This can lead to creep power law breakdown [20] during the hold period, which is not representative of the operating conditions of an IHX. Additionally, the holding stress corresponding to the peak strain reduces every cycle due to cyclic softening. This makes the calculation of creep damage fraction cumbersome.

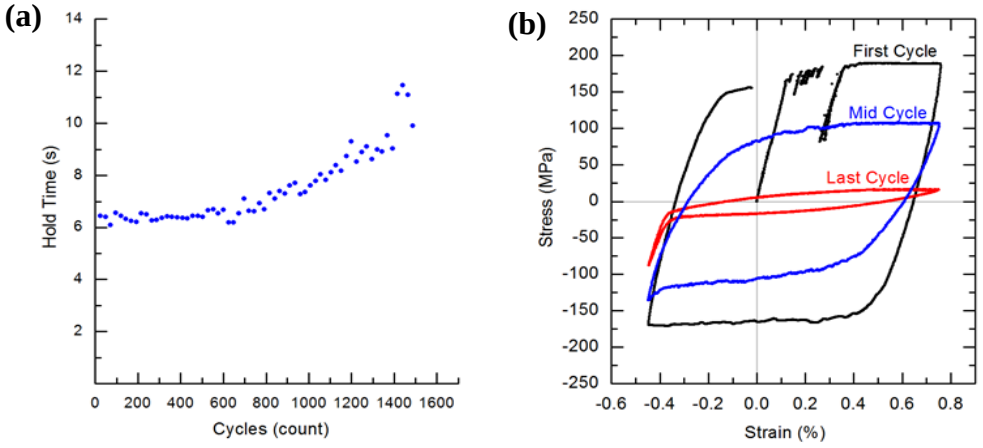

Fig. 2.3 – (a) Stress strain curves for first, mid and last cycle; (b) Increase in hold time with cycles due to softening.

2.2.3 Hybrid-Control with Hold at Intermediate Stress

In time fraction approach, the creep fraction can be varied by changing the hold time and hold stress, whereas the fatigue fraction can be varied by changing the fatigue strain range. A loading profile in which the stress is held constant at an intermediate stress level instead of the stress corresponding to peak strain can allow more flexible control over the creep and fatigue fractions in a test. Moreover, the stress hold does not have to be above the yield stress for the material. This type of loading waveform is also closer to actual service conditions of a heat exchanger where a transient period produces peak stresses, but steady state operation results in intermediate stress levels [21]. Fig. 2.4(a) shows an example of such a loading waveform. The strain is ramped up at a rate of $1x10^{-3}$/s to 0.4%. Following this, strain is reduced until stress is 85MPa and the control is switched from strain to force. Next, the corresponding force is held constant for 10s and the strain is reversed to -0.4% in strain control. This cycle is repeated until failure. Creep hold time per cycle is fixed, the creep strain per cycle increases due to softening as indicated by Fig. 2.4(b).

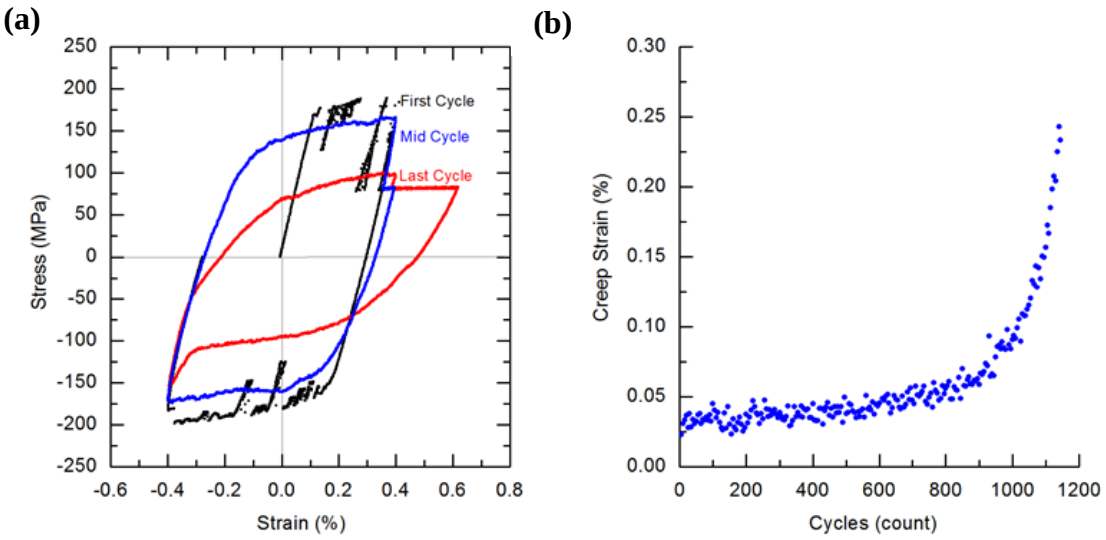

Fig. 2.4 – (a) Stress-strain curve for loading waveform with a 10s hold at 85 MPa; (b) Creep strain increasing with cycles for a fixed hold time of 10s.

In the above loading waveform, stress is held constant for a fixed time each cycle. Another variation of this loading profile is one in which stress is held constant up to a fixed strain each cycle. Fig. 2.5(a) shows a loading waveform with a hold at intermediate stress until a fixed strain of 0.2% is accumulated. Creep strain per cycle is fixed, the hold time per cycle decreases with cycles as indicated by Fig. 2.5(b). Unlike the fixed hold time test, where $\Sigma t_h = n.t_h$, the variation of hold time with cycles must be known to find creep damage fraction in this case.

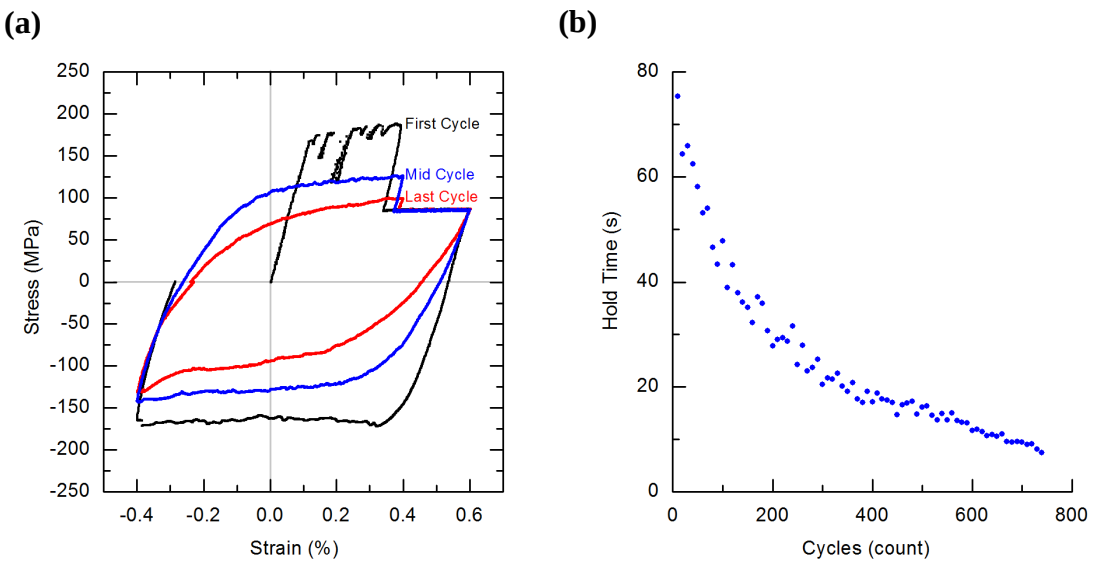

Fig. 2.5 – (a) Stress-strain curve for loading waveform with an 85 MPa stress held constant up to a strain of 0.2%; (b) Hold time decreasing with cycles for a fixed creep strain of 0.2%.

In the aforementioned tests, the value of creep damage fraction was greater than unity. A possible explanation for this result can be the complete reversal of fatigue strain amplitude, which prohibits the accumulation of creep strain with increasing cycles.

2.2.4 Hybrid-Control with Ratcheting and Intermediate Stress Hold

In hybrid-control tests, the fatigue strain range $\Delta\varepsilon_f$ is completely reversed so the creep strain cannot accumulate with cycles. In contrast, for force-controlled tests the creep strain can accumulate with cycles due to ratcheting. The hybrid-controlled loading profile can be modified in such a way that the peak and valley strains increment by a fixed amount each cycle as shown in Fig. 2.6. Since the total strain to failure is approximately 50% and each cycle increments the peak strain by x%, the cycles to failure, *n*, for these tests can be controlled by changing the strain increment, *x*. Therefore,

the fatigue fraction can be treated as a control variable, whereas the creep fraction is the response. It was hypothesized that controlling the fatigue fraction would help in achieving a value of creep fraction that is less than unity.

In this test strain was ramped up at a rate of $1x10^{-3}$/s to 0.4%; strain is reduced until the stress is 85MPa; stress is maintained at 85MPa in force-control until the strain reaches 0.6%; strain is reversed to -0.2% in strain control; Strain is ramped up to 0.6% and the steps are repeated. This leads to a fatigue strain range of 0.8% and a creep strain of 0.2% per cycle.

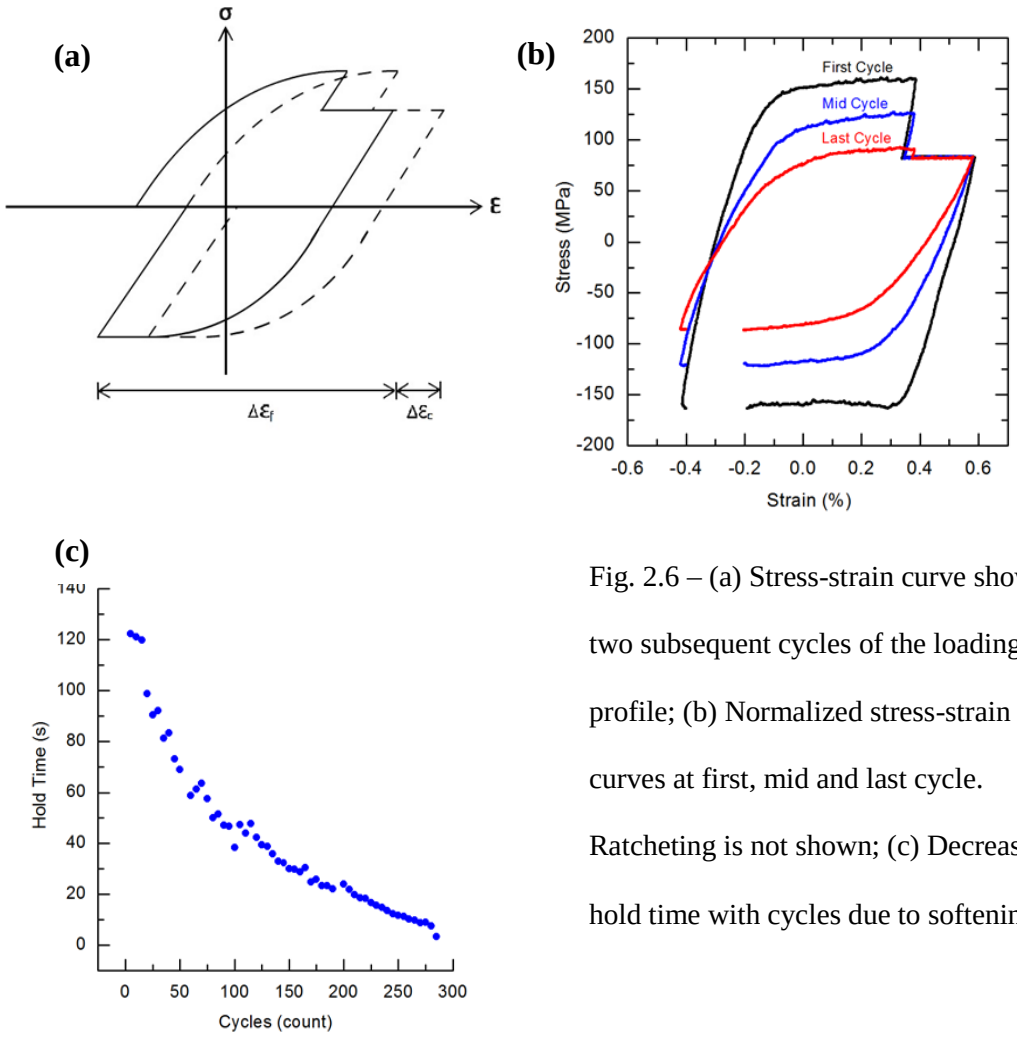

Fig. 2.6 – (a) Stress-strain curve showing two subsequent cycles of the loading profile; (b) Normalized stress-strain curves at first, mid and last cycle. Ratcheting is not shown; (c) Decreasing hold time with cycles due to softening.

In this loading profile, creep fraction is very large due to the ratcheting, which indicates that this loading waveform may not be suitable for producing creep-dominant creep-fatigue interaction data. Thus, this loading profile has similar limitations as purely stress-controlled testing.

2.3 RESULTS AND DISCUSSION

A summary of different types of loading profiles is shown in Table 2.1, each with their unique pros and cons. Some tests are fully strain-reversed and some are fully stress-reversed. For the objective of this study, the hybrid control test with intermediate stress hold (either for a constant time or to a constant strain) is considered to be the optimal testing procedure due to: 1) its flexibility in generating the full range of test runs with varying contributions of creep and fatigue damage by changing the creep holding stress, hold time (or creep strain) and fatigue strain range; 2) absence of ratcheting damage; 3) its creep holding stress being less than the yield stress which is a realistic loading state for the power plant.

Testing profiles	Fully reversed strain	Fully reversed stress	Cyclic ratcheting	Creep-Fatigue Interaction	Comments
Purely strain-control with stress relaxation	Yes	No	No	Fatigue-dominant only	
Purely force-control	No	Yes	Yes	Creep-dominant only	
Hybrid-control with stress hold at peak strain	Yes	No	Yes	Creep-dominant only	Creep power law breakdown; not representative of operating conditions
Hybrid-control with intermediate stress hold	Yes	No	No	Full range of creep fatigue contributions	More representative of operating conditions
Hybrid control with ratcheting and intermediate stress hold	No	Yes	Yes	Creep-dominant only	Large ratcheting damage in addition to creep/fatigue

Table. 2.1 – Comparison of creep-fatigue loading waveforms and their capacity to generate the full range of creep-fatigue interaction.

Thus, additional tests were performed using the hybrid-control loading waveform with a hold at intermediate stress. The test results are summarized in Table 2.2. Creep damage fractions were calculated using the time fraction approach and fatigue damage fractions were calculated as cycle fractions as shown in Eq. 1.

#	Fatigue Strain Range %	Fatigue Stress Range MPa	Holding Stress MPa	Hold Times s	Creep Strain %	Cycles to Failure	Comments
1	0.80	-	85	10	-	1145	Fixed Hold Time
2	0.80	-	85	120	-	200	
3	0.80	-	85	150	-	150	
4	0.80	-	85	180	-	180	
5	0.80	-	85	900	-	33	
6	0.60	-	100	900	-	12	
7	0.60	-	100	180	-	94	
8	0.60	-	100	30	-	480	
9	0.80	-	85	-	0.20	850	Fixed Creep Strain
10	0.80	-	85	-	0.30	560	
11	0.80	-	70	-	0.20	600	
12	0.80	-	70	-	0.30	340	
13	1.00	-	85	-	0.20	630	
14	1.00	-	85	-	0.30	450	
15	-	80	40	30	-	15000	Force-Controlled Tests
16	-	110	55	30	-	7886	
17	-	140	70	30	-	1470	
18	0.90	-	Peak	-	0.30	690	Hold at Peak Strain
19	0.80	-	85	-	0.20	251	Ratcheting by 0.2%
20	0.80	-	-	-	-	1670	Pure Fatigue
21	-	-	85	-	-	11200s	Pure Creep

Table 2.2 – Summary of test results

The results are presented on creep-fatigue interaction diagram in Fig. 2.7. In traditional strain-controlled creep-fatigue testing for Alloy 617, the fatigue damage fraction (usually between 0.3 and 0.7) is larger than the creep fraction (usually in the range of 0-0.2). For the proposed testing profiles, the results are very different. The tests

have large creep fraction (ranging from 1.5 to 4.5) and a relatively small fatigue fraction (mostly falling between 0 and 0.5). A creep fraction larger than unity has been reported in the literature for steels [14,21,22]. It is also interesting to note that, using the new testing profiles, creep fraction does not increase monotonically with increasing hold time. This contradicts the common expectation that a longer hold time will lead to higher creep damage fraction. The absence of a clear trend combined with large values of creep fraction mean that damage summation and time fraction approach are not sufficient for creep-fatigue life prediction for this new loading profile. A detailed explanation requires further experiments and analysis. The authors suspect this phenomena is due to the following reasons: (i) existing life prediction models with time fraction approach are more suitable for strain-controlled loading waveforms; (ii) creep-fatigue interaction is strongly dependent on the type of loading waveform used [21] so different loading waveforms may follow different interaction curves; (iii) the definition of creep damage fraction as a ratio of cyclic hold time and creep rupture time is not appropriate since creep strain in creep-fatigue tests does not accumulate monotonically (i.e., in the case of creep rupture testing) with cycles due to the strain reversal. The above statements would imply that a new life-prediction methodology must be proposed to accurately predict life for both strain-controlled and hybrid-controlled loading profiles.

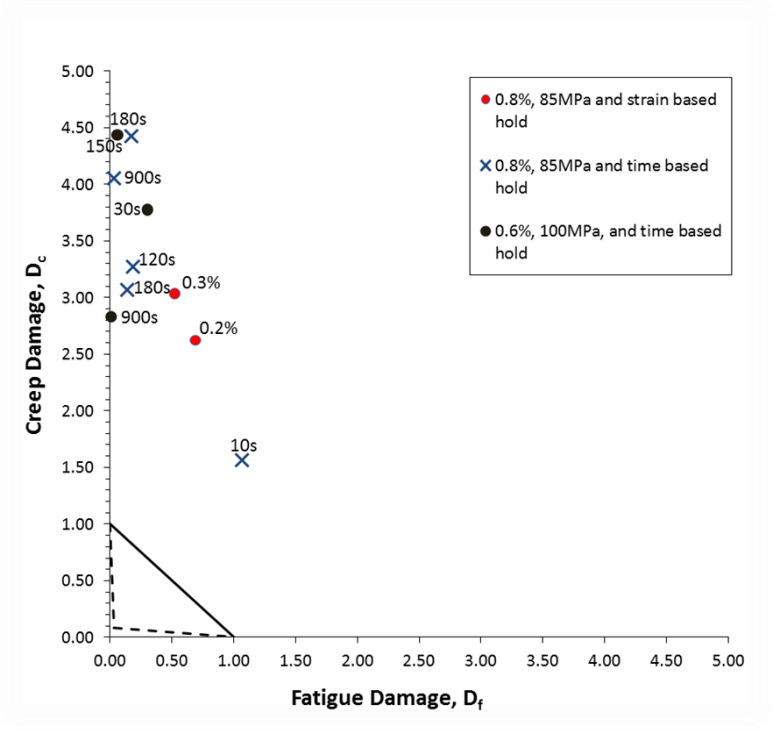

Fig. 2.7 – Creep-fatigue damage interaction diagram for hybrid-control tests with hold at intermediate stress.

2.4 CONCLUSION

A new testing profile for generating creep-dominant creep-fatigue interaction is proposed in this paper and it is fundamentally different from the traditional strain-controlled fatigue-stress relaxation tests. The major conclusions from this experimental study are:

- Pure force-controlled tests only produced extremely ‘creep-dominant’ interaction for Alloy 617 at 950°C and did not produce data in the regime of creep-fatigue interaction;

- When Alloy 617 was subjected to novel loading waveforms - with a combination of force and strain control at 950°C, the creep damage fraction as estimated by the time fraction rule was greater than unity;
- Experimental results from the new loading profiles did not show clear and monotonic trends on the creep-fatigue damage interaction diagram;
- Classical creep-fatigue life prediction models are based on strain-controlled tests and cannot be extended to non-standard loading waveforms.

The damage interaction diagram based on time fraction rule - currently suggested by Boiler and Pressure Vessel Code [23] – is not valid for creep-fatigue life prediction under unconventional loading waveforms. Hence, further experiments and analytical study are required to develop a new creep-fatigue damage interaction diagram for design purposes. The new diagram must work for the proposed loading waveforms as well as the traditional strain-controlled testing. Moreover, a mechanism investigation of microstructural damage evolution may be conducted to reveal any correlations between local damage features and the applied loading waveforms. A life prediction model which utilizes a damage interaction diagram based on micro-scale damage evolution mechanisms will be valuable for a complete understanding of the proposed testing profiles and creep-fatigue failure of Alloy 617 at elevated temperatures.

3. IMAGE-BASED CREEP-FATIGUE DAMAGE MECHANISM INVESTIGATION

3.1 INTRODUCTION

Creep-fatigue interaction can be explained microstructurally as a combined effect of creep and fatigue damage, where creep mainly produces internal voids while fatigue generates surface cracks [1]. Alloy 617 contains M_6C and $M_{23}C_6$ type carbides, where $Cr_{23}C_6$ constitutes a large portion of the grain boundary and twin boundary precipitates [24]. These precipitates provide creep resistance by preventing grain boundary sliding, and they also act as void nucleation sites. Under creep-fatigue conditions, multiple voids initiate and coalesce along the grain boundaries and eventually interact with surface cracks to accelerate intergranular crack growth [16]. Alloy 617 is also known to form a layer of Cr_2O_3 on the surface of test specimens in air at elevated temperatures and the thickness of this oxide layer is a function of time and temperature [25]. Underneath the surface oxide layer is a sub-layer consisting mainly of Al_2O_3 precipitates [8] and a decarburized region due to the oxidation of chromium carbides [26]. Surface cracks are typically flanked by a Cr rich oxide layer [7]. Dynamic recrystallization[25] and precipitate redistribution[27] have also been studied for Alloy 617 at temperatures of 800-1000°C. Studies on microstructural damage induced in Alloy 617 under strain-controlled creep-fatigue loading at 950°C observe large amounts of grain-boundary cracking but negligible cavitation, especially for longer hold times [8,16]. The absence of creep voids coupled with internal grain boundary cracking [8] indicates that purely strain-controlled loading causes fatigue-dominated failure for Alloy 617 at 950°C. This can be explained

by rapid stress relaxation of Alloy 617 at high temperatures which implies that increasing hold time will not increase the creep damage fraction in the strain-controlled testing [6,7]. This study employs a loading profile with force-controlled hold periods [28] to generate a larger proportion of creep damage, thereby allowing tests to cover the entire range from fatigue dominated to creep dominated failure.

Fatigue life at elevated temperatures is influenced by strain rate, hold time, type of hold – stress or strain, and type of loading waveform [1,21]. Existing creep-fatigue design curves for Alloy 617 are derived from tests with strain-controlled loading profiles [7,9]. These design curves are based on damage summation rule using the time fraction approach, which is inadequate for life prediction of Alloy 617, regardless of the loading profile (i.e. strain-controlled or force-controlled hold periods) [6,28]. Moreover, the widely used damage diagram (D-diagram) is a phenomenological representation of macro level testing data. An accurate D-diagram should be directly supported by the underlying microstructural damage mechanisms, which is currently lacking in the open literature. Thus, there is a need for a creep-fatigue life prediction methodology that is informed by an analysis of microstructural damage features. The objective of this study is to qualitatively and quantitatively investigate the microstructural failure mechanisms using imaging analysis. The imaging analysis results are compared with the macro-level loading parameters, both from classical creep-fatigue damage summation rule suggested by the ASME Boiler and Pressure Vessel Code [9] and a newly proposed approach based on correlational analysis.

The paper is organized as follows. First, the experimental testing procedure for the new testing profile is discussed along with testing matrix, and specimen preparation. Next, qualitative imaging interpretation is given for the damage features observed and their relationship with loading conditions. A quantitative statistical analysis is performed to extract the fatigue crack length distribution and interval void density distribution information. The statistical information is then compared with the classical time fraction approach for life prediction suggested in ASME codes. Following this, the same testing procedure is applied to a set of interrupted test specimens and time-dependent micro-scale damage evolution is investigated. Finally, some conclusions and future work are drawn based on the proposed study.

3.2 EXPERIMENTAL TESTING AND IMAGING ANALYSIS

3.2.1 Testing Setup and Procedure

Creep-fatigue tests were carried out on a servo-hydraulic load frame equipped with a three-zone furnace. Furnace temperature was maintained at 950°C for the duration of each test. The test specimens had a circular cross-section, button-head ends, and tangentially blended fillets between the test section and ends, in accordance with ASTM 2714-13. The specimen had a gage length of 20mm and reduced section diameter of 7.5mm. The temperature difference along the gage length was maintained below 10°C with the aid of four thermocouples wrapped on to the specimen. Strain was measured by an extensometer with ceramic extension rods that remained in contact with the specimen during the test.

The loading profile for the tests was different from the classical strain-controlled stress relaxation testing. Fig. 3.1 shows the creep-fatigue loading waveform [28] that was used for the tests. The ramps are strain-controlled at a constant rate of $1x10^{-3}$/s, whereas the hold is force-controlled. Combinations of fatigue strain range, holding stress, and hold time were applied to generate varying proportions of creep and fatigue damage. In this study, the testing matrix was designed by varying the fatigue strain range (0.6% and 0.8%), holding stress (85 MPa and 100 MPa), and holding time (30 s, 180 s and 900 s).

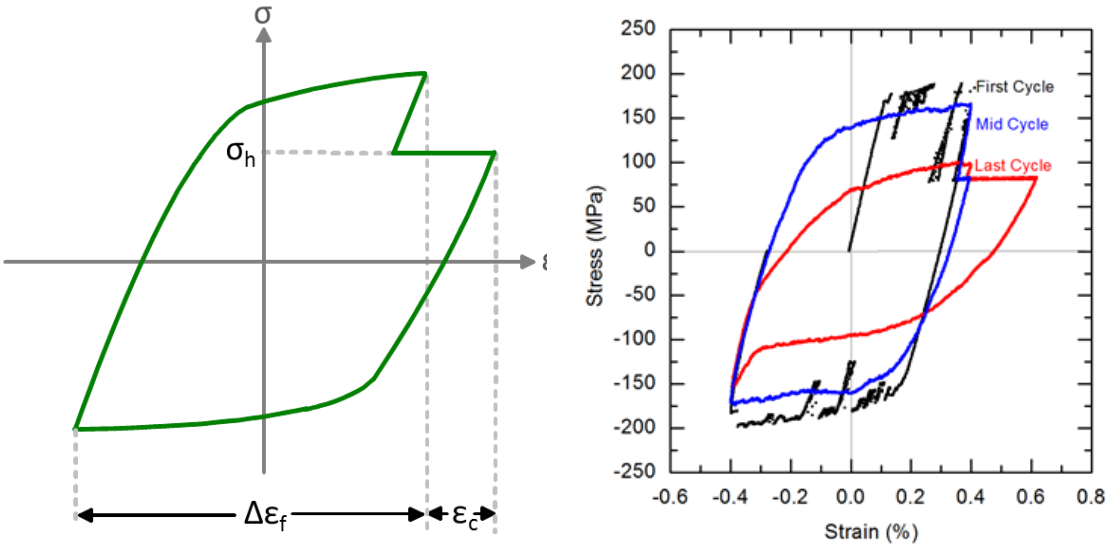

Fig. 3.1 – (a) A schematic of the loading waveform; (b) Loading waveform for first, mid and last cycle for a test with 0.8% fatigue strain range and a 10s hold at 85 MPa;

Ruptured test specimens were split in half along the longitudinal axis using Electric Discharge Machining (EDM). The flat side of the sectioned specimens was initially ground with silicon carbide grit papers ranging from 240 to 1200 grit and subsequently polished with 1 micron polycrystalline diamond suspension on a polishing

pad. The specimens were then examined under Scanning Electron Microscope (SEM) to obtain qualitative and quantitative information about creep-fatigue damage.

3.2.2 Qualitative Image Analysis for Mechanism Investigation

Qualitative image analysis of failure patterns, microstructural damage features, grain structures, and elemental analysis were performed. The failure surfaces were investigated first. There are generally two distinct failure patterns observed in the test specimens. One pattern is associated with significant necking and cup-shape failure surface. The failure surface is very rough indicating ductile rupture. This failure pattern usually occurs with longer hold time and lower fatigue cycles. Another pattern is associated with less necking and relatively flat failure surface. The fracture surface is relatively smooth and shows classical failure characteristics of brittle fatigue fracture. This failure pattern usually occurs with shorter hold time and higher fatigue cycles. Fig. 3.2 shows tests specimens with the abovementioned failure patterns. This observation strongly suggests that there are at least two failure modes in this testing: one is creep rupture-dominated and the other is fatigue fracture-dominated.

(a) (b) (c)

Fig. 3.2 – Optical images of the sectioned test specimens for 0.8% fatigue strain range and 85 MPa holding stress with (a) 30 s holding time; (b) 180 s holding time; (c) 900 s holding time.

Following this, the SEM images for all failure specimens are taken and observations focused on the internal voids and surface cracks. The representative results are shown below with respect to different holding time. Fig. 3.3 shows the 900 s hold time test resulted in creep dominated failure as evidenced by large voids which showed signs of coalescence. Surface cracks are shorter and tend to link with the sub-surface voids (Figs. 3.3(a) and 3.3(b)). Many internal voids are initiated and are linked together to eventually break the specimen. Fig. 3.4 shows the 180 s hold time test which also produced both voids and cracks, but there was minimal interaction between them. The average crack length is longer than that observed for 900 s hold and the average void density is smaller than that observed in 900 s hold (quantitative statistical analysis will be shown later). Fig. 3.5 shows the 30s hold time test, which resulted in fatigue dominated failure indicated by the long surface cracks, some internal cracks and no voids (or the voids are smaller than the current resolution allows i.e. diameter > 1~2 μm). The long

surface cracks appear to show a mix of inter-granular and trans-granular crack growth. In general, the surface cracks become more straight and perpendicular to the applied loading direction in 900 s hold test than that in the 30 s hold test (see Figs. 3.3-3.5). This observation suggests that the fatigue crack propagation tends to be more trans-granular when the holding time decreased. This can be explained by the weakening of grain boundaries by the creep voids. As most internal voids lie on the grain boundaries, significant creep damage will make the fatigue crack propagate along the weakened grain boundaries. If the grain boundary is not weakened significantly (i.e., lower hold time and creep damage), the fatigue crack will propagate as trans-granular cracks.

The crack surfaces were oxidized (see Fig. 3.5(c) and 6(d)) which is due to the long exposure time of fatigue crack surfaces under high temperature conditions. EDS results will be shown later to confirm the oxidization by elemental analysis. Grain boundary cracks in the interior of the specimen were only observed in fatigue dominated case and it is known that strain-controlled creep-fatigue testing on Alloy 617 at 950°C tends to generate interior grain boundary cracks instead of large voids [8]. This implies that most strain-controlled creep-fatigue tests lie in the fatigue dominated failure regime.

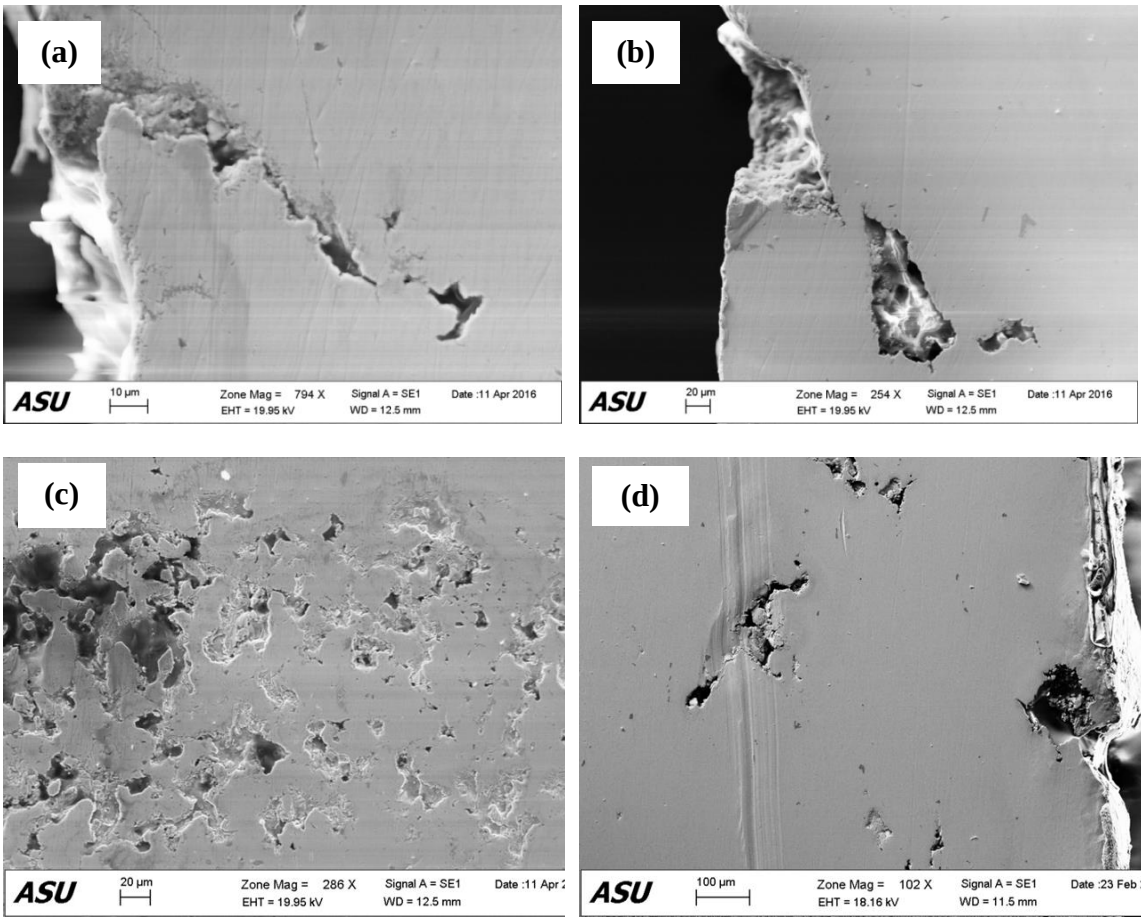

Fig. 3.3 – Test specimen with creep dominated failure (i.e. 900 s hold) shows (a), (b) linkage of surface cracks with sub-surface voids; (c) , (d) extensive void coalescence near fracture surface.

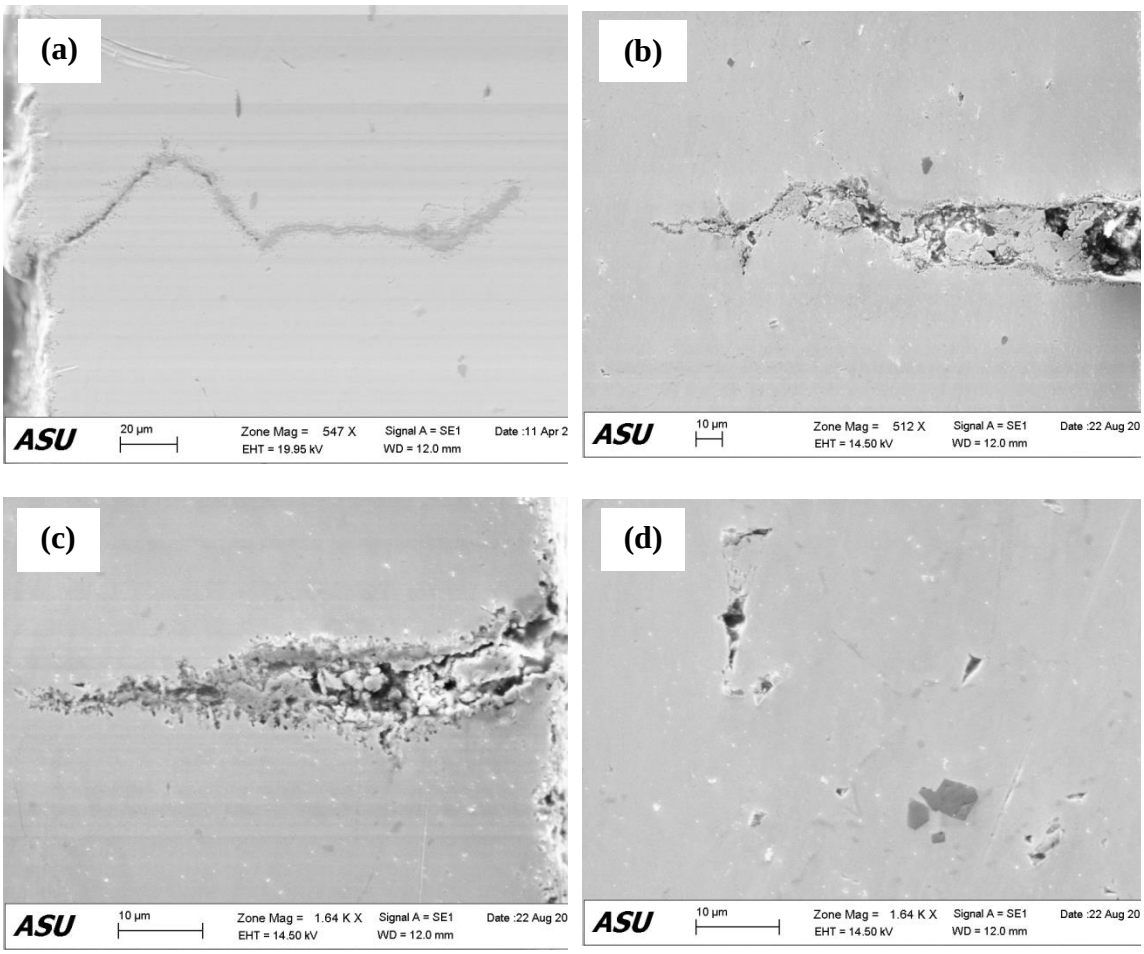

Fig. 3.4 – Test specimen with creep-fatigue interaction failure (i.e. 180 s hold) shows (a) mixed inter- and trans-granular crack growth (b), (c) transgranular cracks and (d) voids concentrated near the specimen surface.

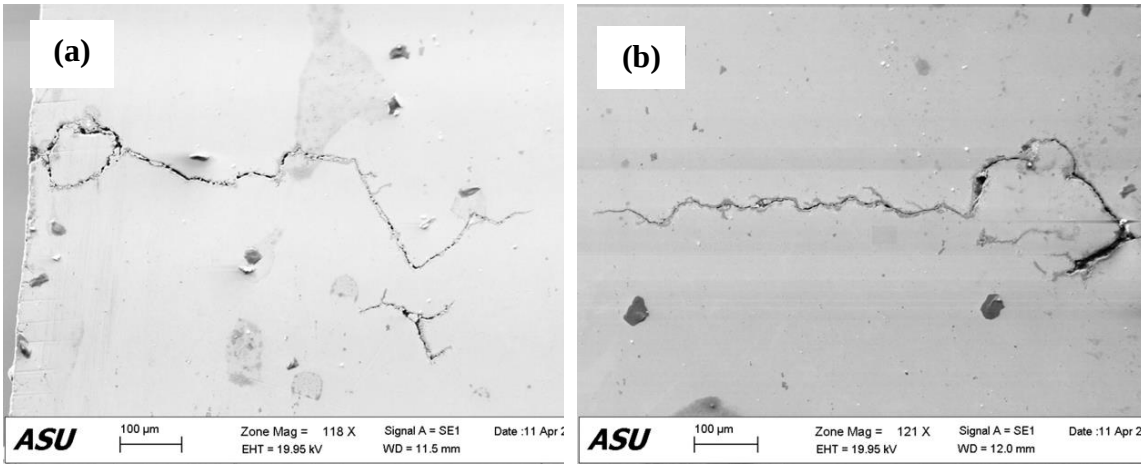

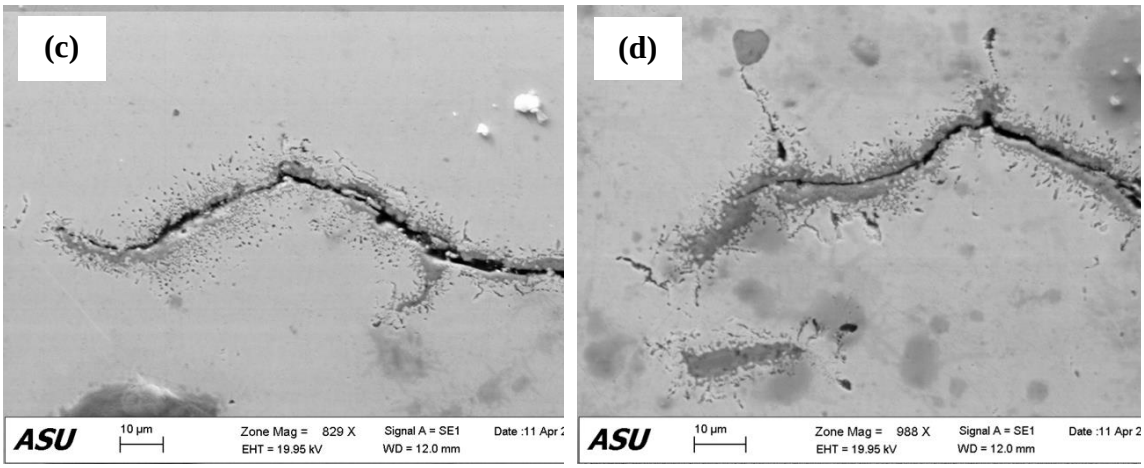

Fig. 3.5 – Test specimen with fatigue dominated failure (i.e. 30 s hold) shows (a), (b) long intergranular cracks; (c), (d) thin o layer flanking the cracks and grain boundaries ahead of the crack tip.

Next, Electron Backscatter Diffraction (EBSD) was used on a specimen with creep dominated failure to identify the grain structure with respect to damage. It is observed that most internal voids are on the grain boundaries. An example is shown in Fig. 3.6. SEM images were obtained to identify the region of interest (ROI) with voids. The EBSD images for the ROI were then compared / overlapped with the SEM images. It is clear that the voids were generated at the grain boundaries (GB), especially near triple junctions and GBs with high misorientation angles. The voids tend to grow along the GB and link with the neighboring GB voids.

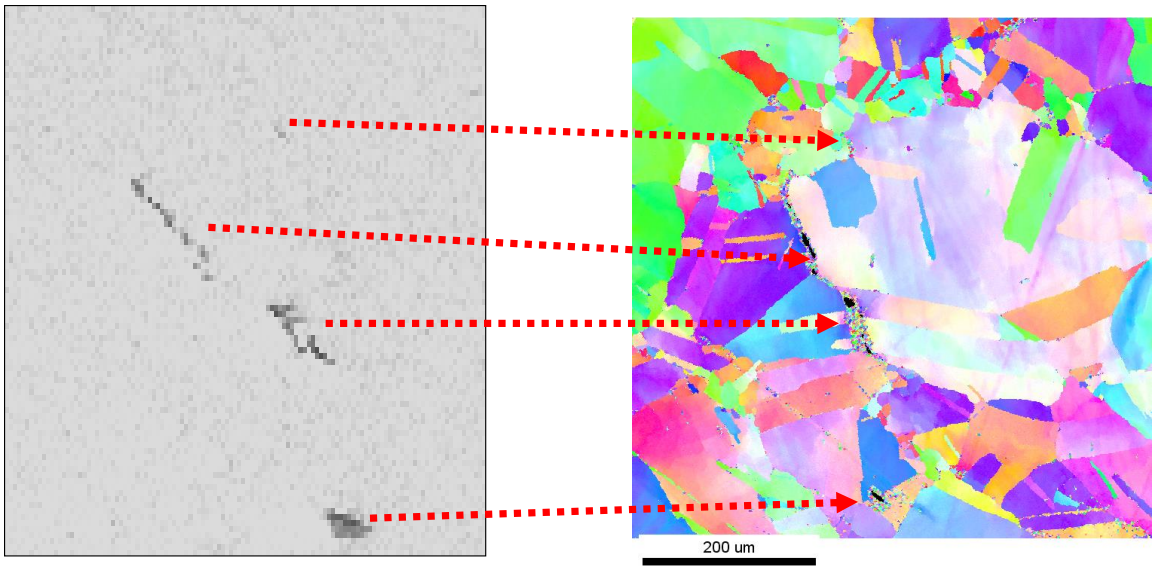

Fig. 3.6 – SEM and EBSD imaging for internal voids of failed specimen

Following this, Energy Dispersive Spectroscopy (EDS) was used to identify the elements near the fatigue cracks. Fig. 3.7 show an EDS phase map for a test specimen with 0.6% fatigue strain range, 100 MPa holding stress, and 30 s hold time. This condition represents fatigue dominated failure for current loading profile. The crack surfaces were flanked by an external layer of chromium oxide and an internal layer of aluminum oxide. The precipitates were titanium nitride. In contrast to the fatigue dominated test specimen, the creep dominated specimen showed blunt cracks with no oxidation layer. This indicates that creep dominated specimens developed surface cracks near the end of the cycle life, whereas fatigue dominated specimens developed surface cracks early on, allowing sufficient time for the exposed surfaces to oxidize. The EDS composition map is shown in Fig. 3.7.

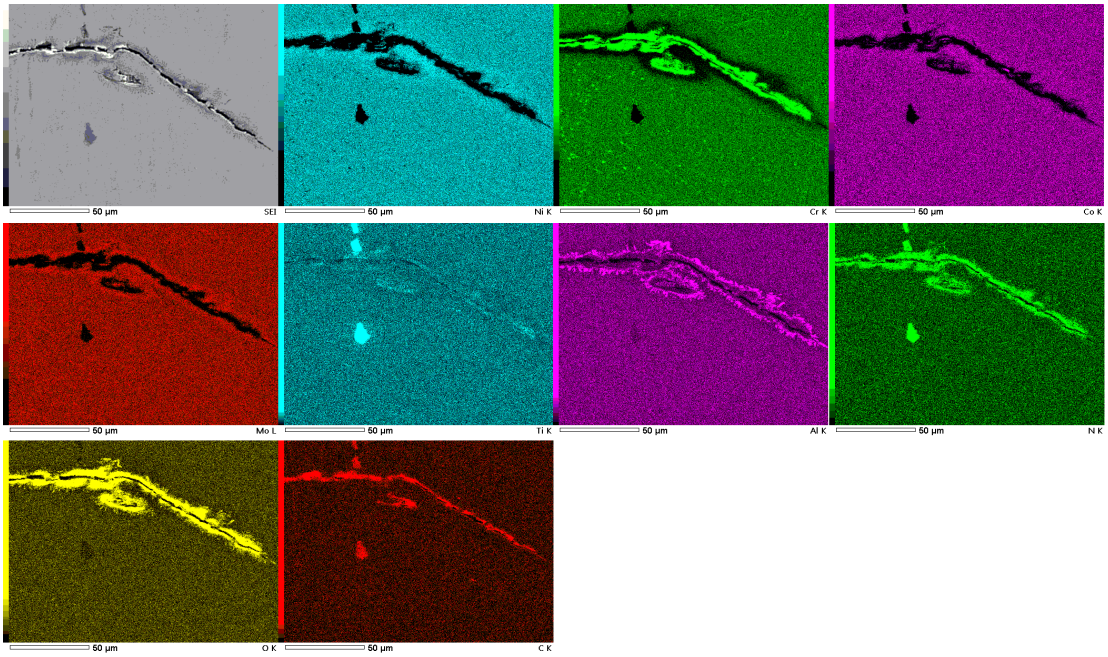

Fig. 3.7 – EDS phase maps for surface crack on a test specimen with fatigue dominated failure

Fig. 3.8 compares the relation between cycle life and hold time for hybrid-control and strain control tests. In traditional strain-controlled creep-fatigue tests, increasing the hold time does not lead to increase in creep damage, due to rapid stress relaxation of Alloy 617, as shown in Fig. 3.8(b). However, hybrid-control tests show a reduction in cycle life with increase in hold time, as shown in Fig. 3.8(a). Generating creep dominated damage is one of the main advantages of using a hybrid-control loading profile. Micro-scale image analysis provides physical evidence for this behavior. Specimens undergoing hybrid-control loading show that longer hold time does leads to more creep damage as characterized by void initiation and coalescence at grain boundaries whereas shorter hold time leads to fatigue dominated damage as represented by oxidation-assisted crack growth at exposed outer surfaces.

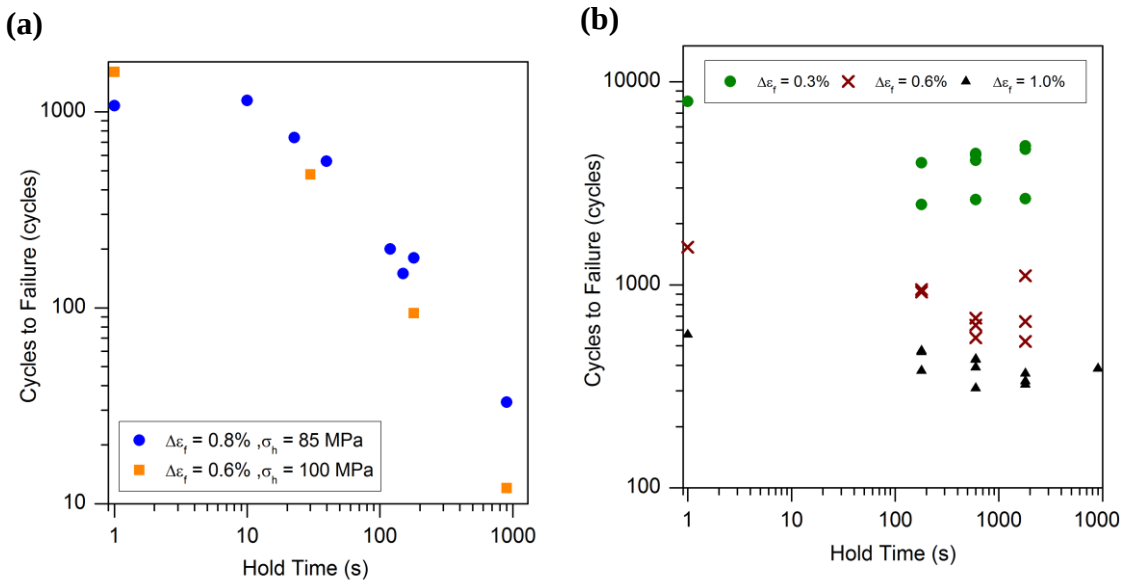

Fig. 3.8 – Relation between cycle life and hold time for (a) hybrid-control tests; (b) strain-control tests [29].

3.2.3 Digital Imaging Measurements and Statistical Data Analysis

Above discussion was interpretation of imaging for experimental observations of a new testing profile that is capable of producing creep dominated failure. It provides insights into the damage mechanisms involved, but does not provide quantitative measurements for future life prediction models and design curves. Thus, this section focuses on digital imaging measurements and statistical data analysis to achieve this goal. The focus is on the following metrics: surface crack length, number of voids, and void area / area fraction.

The new hybrid-control creep-fatigue tests covering a range of creep and fatigue fractions were used for image-based damage analysis in SEM. The length of each surface crack along the gage length of the specimen was measured in SEM to provide an estimate

of fatigue damage. Fig. 3.9 shows the tail of an empirical cumulative distribution function of the crack lengths from three tests with a fatigue strain range of 0.6%, a holding stress of 100 MPa and hold times of 30, 180, and 900s, respectively. The distribution of crack lengths less than 200μm was almost identical for the three tests. However, the 10% percentile curves for cracks with lengths greater than 200μm showed significant differences between creep dominated and fatigue dominated failure modes. In this case, 30s hold time represents fatigue dominated failure whereas a 900s hold time represents a creep dominated failure. The fatigue dominated case has much longer crack lengths compared to the creep dominated case. It should be noted that the mean crack length is not compared here as the failure is an extreme event and only the tail region (i.e., longest cracks in the specimen) affect the final failure. In the current investigation, the longest crack observed in the fatigue dominated specimen is about 10 times the length of the longest crack in the creep dominated case. The mean and standard deviation of the measured cracks are shown in Table. 3.1. It is observed that, not only the mean crack length, but also the standard deviation of the crack length increases as the hold time decreases.

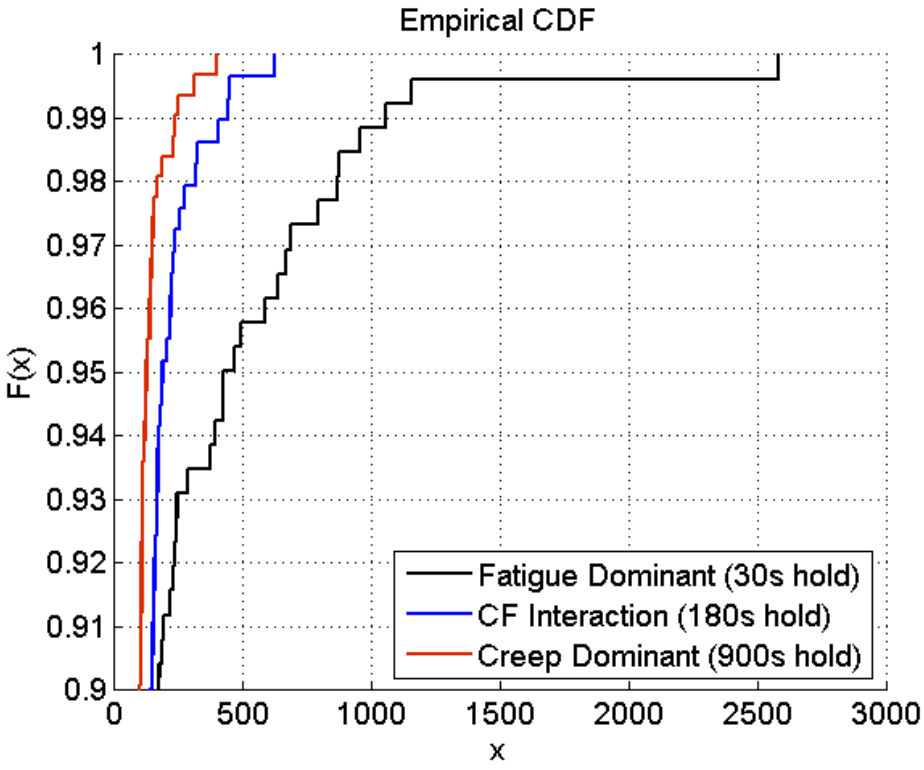

Fig. 3.9 – Empirical cumulative distribution function (F(x)) for length of surface cracks (x) during creep-fatigue tests with varying hold time

Hold Time, s	**Mean Crack Length (μm)**	**Standard Deviation (μm)**
30	94.05	230.62
180	69.06	76.30
900	51.59	47.80

Table. 3.1 – Mean crack length and standard deviation corresponding to different hold times

The next digital measurements were for the internal voids. Multiple SEM images were captured across the width of the specimen at distances of 1mm, 3mm and 5mm from the rupture surface, as shown in Fig. 3.10. The reason is that the internal void distribution is not uniform across the length of the specimen. Image analysis was performed to determine the ratio of area covered by voids to the total area in the image. This void area fraction was used as an indicator of creep damage in the sample. Fig. 3.10 summarizes the void damage in a test specimen with creep dominated failure i.e. 0.6% fatigue strain range, 100 MPa holding stress, and 900 s hold time. The results of image analysis for this particular sample are shown in Table 3.2. The area fraction of voids and average void size was highest near the rupture surface but the number of voids was lowest, indicating that final failure was caused by void coalescence. Only voids larger than 1 μm were analyzed. A similar analysis was performed on the fatigue dominated test specimen with 30 s hold time and creep-fatigue interaction test specimen with 180s hold time. No voids larger than 1 μm were detected on the fatigue dominated test specimen with 30 s hold time. For the creep-fatigue interaction specimen, voids were present but their average size and area fraction was less than the creep dominated specimen.

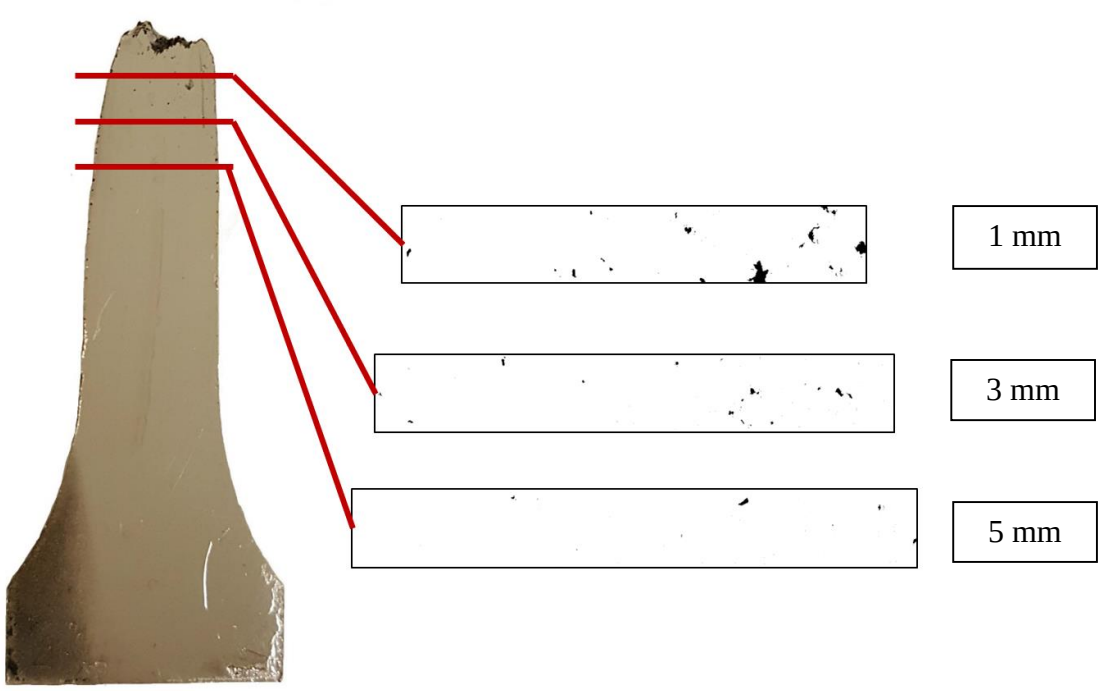

Fig. 3.10 – Analysis of voids on a sectioned half of the ruptured test specimen

Distance from Fracture Surface, mm	No. of Voids	Average Void Size, μm^2	Area Fraction of Voids, %
1 mm	56	1135.88	1.492
3 mm	86	206.96	0.373
5 mm	100	104.24	0.207

Table. 3.2 – Variation in number, size and area fraction for voids at fixed distances from the rupture surface

3.3 CORRELATIONAL ANALYSIS FOR IMAGING MEASUREMENT AND MECHANICAL DAMAGE PARAMETERS

As mentioned in the introduction, one benefit for the rigorous quantitative imaging analysis is that it can provide a statistical correlation with the external damage parameters. Thus, the micro-scale damage features and macro-level damage parameters can be linked. This section focuses on this objective. For the micro-scale damage features, the crack length and void area fraction are selected. For the macro-level damage model, the widely used ASME damage summation rule with time fraction approach is applied. The damage parameters are fatigue fraction (i.e., number of cycles to failure in creep-fatigue testing normalized by the corresponding pure fatigue failure cycles) and creep fraction (summation of hold time normalized by the creep rupture time). It is expected that, if the model is correct, a correlation between the micro-scale features and damage parameters can be identified. The following analyses are done for fatigue and creep correlation, respectively.

If fatigue damage is considered as initiation and propagation of surface cracks and creep damage is considered as initiation, growth, and linkage of voids, then creep-fatigue interaction diagram based on these damage features can provide useful insights for the purpose of developing microstructure-informed creep-fatigue life prediction models. Tests were performed with varying fatigue strain range, holding stress, hold time, and type of hold to generate creep-fatigue interaction. The type of hold refers to whether the force-controlled hold during each cycle was for a fixed time period or up to a fixed strain value. Fig. 3.11 shows a significant variation in crack lengths across different tests for

cracks longer than 200μm. Specimens with larger fatigue damage fraction have longer cracks indicating that crack growth is the primary damage mechanism for fatigue dominated failure. This hypothesis is further supported by the linear increase in mean and standard deviation of crack lengths with increasing fatigue damage fraction, as shown in Fig. 3.12. The fatigue damage fraction was slightly larger than unity for the 10s hold test. This implies that a 10s hold time test is similar to a pure fatigue test and that the 10s hold is not enough to induce creep damage. It is interesting to note that the test with force-controlled hold up to a fixed strain (green circle in plot) does not show significant variation from the linear trend of mean and standard deviation of crack lengths. This analysis indicates that the fatigue fraction is a good candidate for the development of creep-fatigue models as it closely related to the micro-scale damage (crack length and its variance).

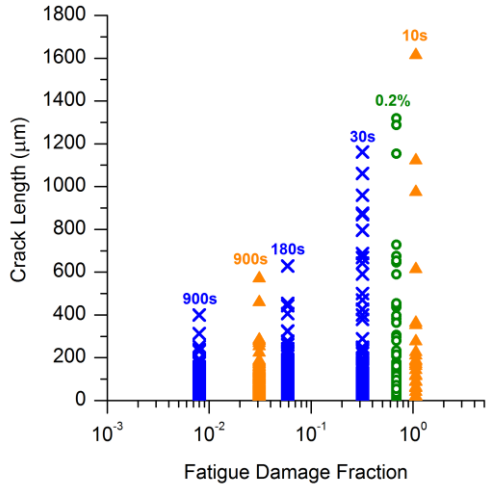

	Fatigue Strain Range (%)	Holding Stress (MPa)	Type of Hold
×	0.6	100	time
▲	0.8	85	time
○	0.8	85	strain limit

Fig. 3.11 – Variation in distribution of crack lengths with fatigue damage fraction. Error bars represent standard deviation.

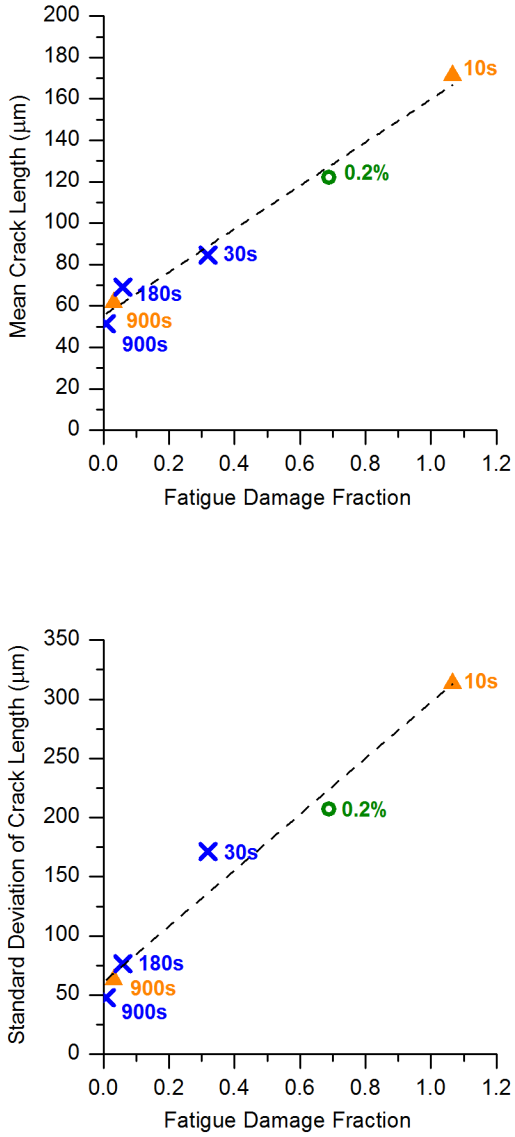

	Fatigue Strain Range (%)	Holding Stress (MPa)	Type of Hold
×	0.6	100	time
▲	0.8	85	time
○	0.8	85	strain limit

Fig. 3.12 – Mean and standard deviation of crack length increase with increasing fatigue damage fraction

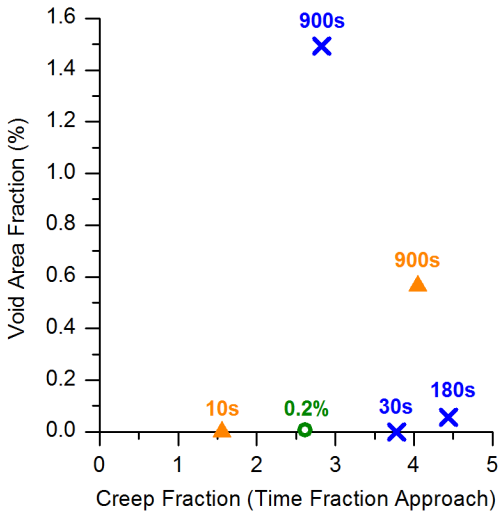

Fig. 3.13 – Relation between void area fraction 1mm below the rupture surface and creep damage fraction using time fraction approach

Next, the correlation is done for the internal void area fraction and creep time fraction. Since the internal voids are not uniformly distributed across the specimen length, the void area fraction was calculated at 1mm distance from the rupture surface, as described in the previous section. Fig. 3.13 illustrates that there is no relation between void area fraction and creep damage fraction calculated using the classical time fraction approach. It is also interesting to note that the 900 s hold (blue circle) has less "creep damage fraction" compared to the 30 s and 180 s hold. This is contrary to expectation and evidence provided by imaging analysis described earlier. This suggests that the widely used time fraction approach for calculation of creep damage is not a good candidate for the creep-fatigue life prediction as it does not correlate well with the damage features; in particular the void area fraction.

Creep-fatigue interaction in steels is traditionally represented by a bilinear trend curve on an interaction diagram that is based on linear damage summation rule and time fraction approach[21,30]. Fatigue damage is represented as a cycle fraction and creep damage is represented as time fraction. Although, the time fraction approach is employed in nuclear component design codes, namely, ASME BPVC Section III Subsection NH[9] and RCC-MR[11], this approach has several limitations[19,31]. Moreover, elevated temperature strain controlled testing of Alloy 617 fails to produce a clear trend on an interaction diagram due to irregular values of creep damage fraction [5,28]. Further theoretical and experimental study is required to find another parameter that is best correlated with the observed internal voids. The current study only investigates a simple alternative mechanical parameter, called effective creep time fraction. The basic idea is briefly discussed here. For the investigated hybrid control loading profile, the total creep strain will monotonically increase from cycle to cycle due to the softening. Thus, the hold time can be divided into two parts: one part is to recover the creep strain happens in the previous cycle and the other part is to increase the creep strain to a new high level. The second part is referred to as the effective hold time and it indicates the time is "effective" in causing monotonic creep strain increment. The summation of this part of hold time for all cycles can be normalized by the creep rupture time and is defined as the effective creep fraction. Fig. 3.14 shows that the observed internal void area fraction has a very good correlation with the effective time fraction definition. It also shows that the creep damage fraction increases as the hold time increases unlike the contradictory results from the classical time fraction approach.

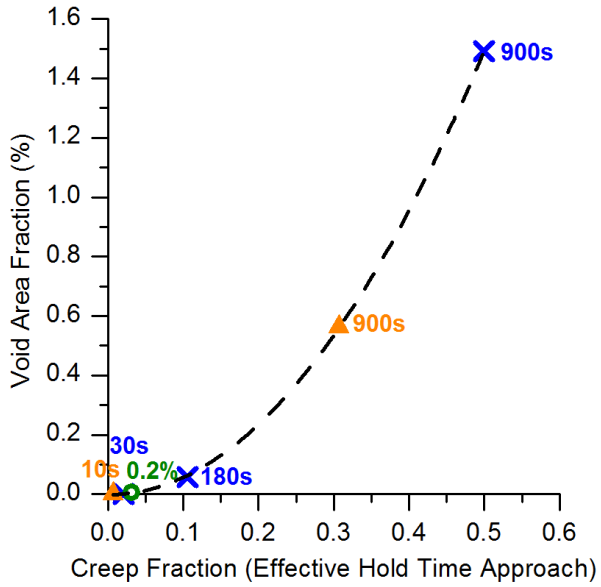

Fig. 3.14 – Correlation between void area fraction and effective hold time creep fraction

Another way to represent the correlational analysis is shown below using the concept of the D diagram. In the D diagram, x-axis represents the fatigue damage and y-axis represents the creep damage. Fig. 3.15 (a) constructs the "D" diagram using the microstructurally observed crack length and void area fraction. Both mean and 90% quantile curves are shown. The micro-scale imaging analysis gives a clear bilinear trend, representing the two distinct failure modes, i.e., creep dominated and fatigue dominated. Fig. 3.15 (b) shows that D diagram using the damage parameters: fatigue fraction and the effective creep fraction. The trend is very similar to the micro-scale imaging results as it also shows a clear bilinear trend. Thus, these two parameters may be used for future life prediction model development as a strong correlation with microstructural damage features is obtained.

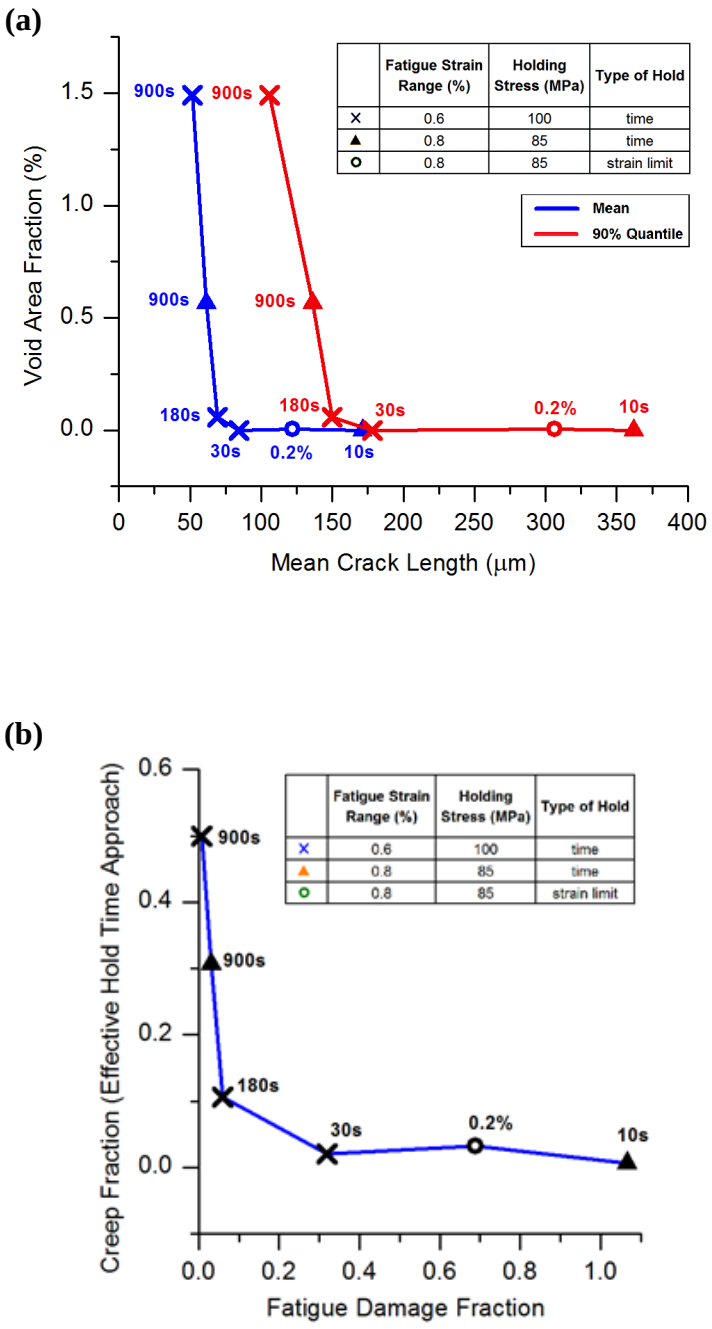

Fig. 3.15 –D diagram construction using micro-scale imaging results and damage parameters (a) Damage interaction diagram based on microstructure; (b) Damage interaction diagram based on effective hold time approach.

3.4 INTERRUPTED TESTING

Interrupted tests were conducted to investigate damage evolution. A creep-dominant creep-fatigue test with 0.6% fatigue strain range, 100 MPa holding stress and 900s hold time was selected for interrupted testing. An initial test was allowed to run till failure to determine the cycle life. The test was then repeated three times and stopped at 25%, 50%, and 75% of the cycle life respectively. Fig. 3.16 shows that the peak and valley stresses for the interrupted tests do not show a significant variation from the initial test.

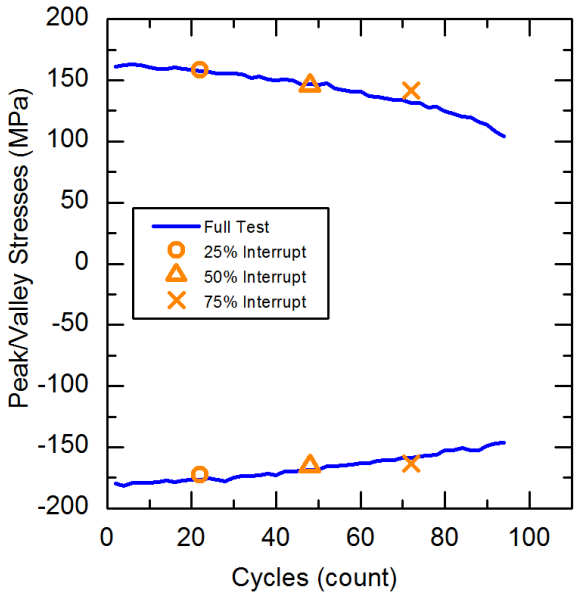

Fig. 3.16 – Peak and valley stresses for interrupted tests

The interrupted test specimens were sectioned along the gage length, polished, and observed under SEM. The length of each surface crack on the gage length was measured. A Kolmogorov-Smirnov test for goodness of fit indicated that a kernel distribution provided the best fit for the crack length data, as shown in Fig. 3.17. Table. 3.3 shows that the mean crack length as well as the standard deviation of the crack lengths increases with

cycles. The exponential increase in standard deviation during the first three quarters of the cycle life can be explained by the initiation of new cracks. The relatively smaller increase in standard deviation during the final quarter indicates that new cracks initiated at a slower rate during this period.

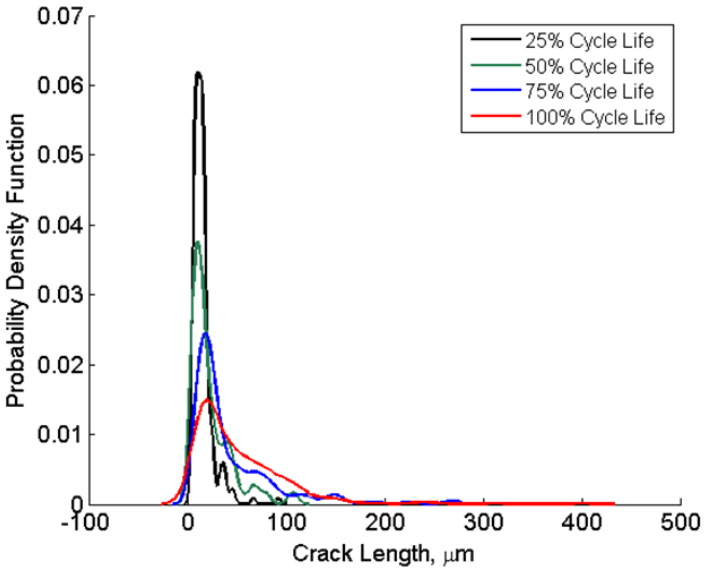

Fig. 3.17 – Probability density function of crack lengths at different interrupts

	Mean Crack Length, μm	**Standard Deviation, μm**
25% Cycle Life	15.40	10.30
50% Cycle Life	23.16	21.06
75% Cycle Life	43.54	44.25
100% Cycle Life	51.59	47.80

Table. 3.3 – Mean crack length and standard deviation at different interrupts

The total number of micro-voids on the gage section of the test specimen was much higher than the number of surface cracks and there was a significant variation in void damage along the gage length. Therefore, an accurate representation of void damage required capturing a large number of high-magnification images covering the entire gage length of the specimen. Since, such a task was beyond the scope of this study, the void damage was studied qualitatively by imaging localized regions of high void density on each specimen and comparing amongst the interrupted tests. Void density was found to be highest near the specimen surface. This can be attributed to oxidation on the surface of the test specimen and consequent decarburization of grain boundary carbides located near the surface. A large increase in mean void size and void area fraction was observed in the last quarter of the cycle life indicating that most of the void growth and coalescence occurred towards the end of the cycle life. This information combined with the crack length analysis shows that, for a creep-dominant test, the damage mechanism changes from crack initiation and growth to void growth and coalescence during the last quarter of the life.

3.5 CONCLUSION

Hybrid-control testing can generate creep dominated failure. Image-analysis confirms that, unlike the classical strain-controlled testing, the new hybrid control testing profile can increase the creep damage by increasing the hold time under force-control. Qualitative image analysis shows that there are two distinct failure modes in the investigated testing cases: ductile creep dominated failure with long hold time and brittle fatigue dominated failure with short hold time. The fatigue crack length correlates well with the cycle number ratios but the void area fraction does not correlate well with the

classical time fraction used by ASME code. An effective hold time approach (i.e. only considering the part of the hold time when net creep strain increase happens) correlates well with the observed void area fraction and provides an alternative way to formulate the damage interaction diagram. These conclusions currently apply to creep-fatigue interaction in Alloy 617 at 950˚C under force-controlled hold periods. A similar analysis can be performed on tests with strain-controlled hold periods, to confirm their inadequacy for generating significant creep damage. Further work may also include the development of a life prediction model, similar to the effective hold time approach, which mimics the bilinear damage curve obtained through micro-scale image analysis.

4. AN EFFECTIVE TIME FRACTION APPROACH FOR CREEP-FATIGUE LIFE PREDICTION

4.1 INTRODUCTION

Accurate life prediction and design methods are critical to ensuring structural integrity and reliability. Nuclear component design codes such ASME-NH [23], RCC-MR [11], and R5 Procedure [12] suggest linear summation of fatigue and creep damage for life prediction. ASME-NH and RCC-MR use a time fraction rule [18,32], where creep damage is represented by a time fraction whereas the R5 Procedure uses a ductility exhaustion concept [33,34], where creep damage is represented by a strain fraction. The parameter that controls creep damage in time fraction approach is stress whereas in ductility exhaustion it is inelastic strain [13,35]. Comparative studies on steels and alloys showed that the time fraction rule underestimates the creep damage leading to non-conservative prediction, whereas the ductility exhaustion approach overestimates the creep damage leading to over-conservative life prediction [13,35]. Another widely studied evaluation method is strain range partitioning [36], which divides the inelastic strain range into three components. This approach requires collecting considerable amount of hysteresis data with specialized loading waveforms [10]. Many other creep-fatigue evaluation methods are available in literature [10,13,31,35,37], but few are simple enough to be considered in design codes [38]. The focus of this study is the time fraction approach, which is preferred by design codes due to its simplicity. Thus, the discussions and comparisons in this paper are aimed at developing a more accurate time fraction approach.

The time fraction approach requires a complete set of creep-fatigue test data for calibration and validation. In open literature, most high temperature creep-fatigue tests are performed using strain-controlled loading waveforms (i.e., fixed strain during hold period leading to stress relaxation). For Alloy 617 at very high temperatures, the rapid stress relaxation generally leads to fatigue dominated damage and therefore makes it difficult to fully calibrate the damage diagram using the time fraction approach [6,13]. Thus, in the current study, a full range of creep-fatigue test data (i.e., both fatigue dominated and creep dominated) at 850°C and 950°C is collected through a newly developed hybrid-controlled loading profile with force-controlled hold periods [28]. Moreover, the experimental data, when plotted using the classical time fraction rule suggested by the draft code case for Alloy 617 [9], shows a significant scatter [39] and non-physical trends (e.g., values of creep damage fraction exceeding unity) [28]. The authors have performed extensive image-based damage analysis and correlational study using scanning electron microscopy of failed creep-fatigue test specimens [40]. It was observed that the microstructural damage features (e.g., microstructural void density) did not correlate with the classical time fraction calculation of creep damage. This observation suggests that other mechanical parameters should be explored to correlate with microstructural damage features and to predict the creep-fatigue life under such loading conditions.

In view of the above discussion, this paper proposes a new life prediction model for calculating creep damage in the particular case of Alloy 617 at temperatures above 850°C. The paper is organized as follows. First, the new experimental procedure for the

hybrid-control creep-fatigue loading [28] and the results of imaging analysis[40] are reviewed and discussed. New tests at 850°C are presented to demonstrate the effect of temperature on the proposed model. Following this, a detailed derivation of the proposed effective time fraction approach is provided for both hybrid-controlled and strain-controlled testing. A comparison with the classical time fraction approach is also given. Next, both in-house data for the hybrid-controlled testing and literature data for the strain-controlled testing are used to demonstrate and validate the proposed life-prediction methodology. Finally, some conclusions are drawn and future work proposed based on the results. The main novelties of the proposed study are: 1) provide a quantitative mechanical model for life prediction using the hybrid-controlled testing profile [28] and evidence from image-based analysis [40]; 2) provide a unified approach for the life prediction using both hybrid-controlled testing and classical strain-controlled testing; 3) check the applicability of the proposed method at both 850°C and 950°C using newly generated experimental data.

4.2 EXPERIMENTAL PROCEDURE AND IMAGING ANALYSIS RESULTS

The authors have developed a new hybrid-controlled testing profile for creep-fatigue testing of Alloy 617 at 950°C [28] and performed imaging analysis for the statistical analysis of micro-scale damage features [40]. Only a brief review of these techniques is given here for the completeness of this study. Detailed discussion and results can be found in the referred articles. Additional experimental testing results at 850°C are presented in this study in order to demonstrate the proposed model at different temperatures**.**

The creep-fatigue tests in this study were run on an MTS servo-hydraulic load frame with a three-zone furnace. The Alloy 617 specimens were machined from a block of raw material such that the rolling direction was parallel to the loading axis of the specimen. The specimens had a round section with button-head ends and tangentially blended fillets at the gage section, in accordance with ASTM 2714-13. The specimen gage length was 20mm and gage section diameter was 7.5 mm.

All tests were performed in air at a constant temperature of either 850˚C or 950˚C. The temperature difference along the gage length was maintained below 10˚C with the help of four thermocouples that were wrapped on to the specimen at different locations. A contact extensometer with ceramic extension rods was used for strain measurement at the gage length. Fig. 4.1 (a) and (b) show the commonly used strain-controlled loading profile where the test specimen undergoes stress relaxation during the hold period. In this study, a hybrid-control loading profile [28] was applied, similar to the one shown in Fig. 4.1 (c) and (d). The loading and unloading was strain controlled at a rate of $1x10^{-3}$ /s, whereas the hold period was force-controlled at a predetermined intermediate stress level.

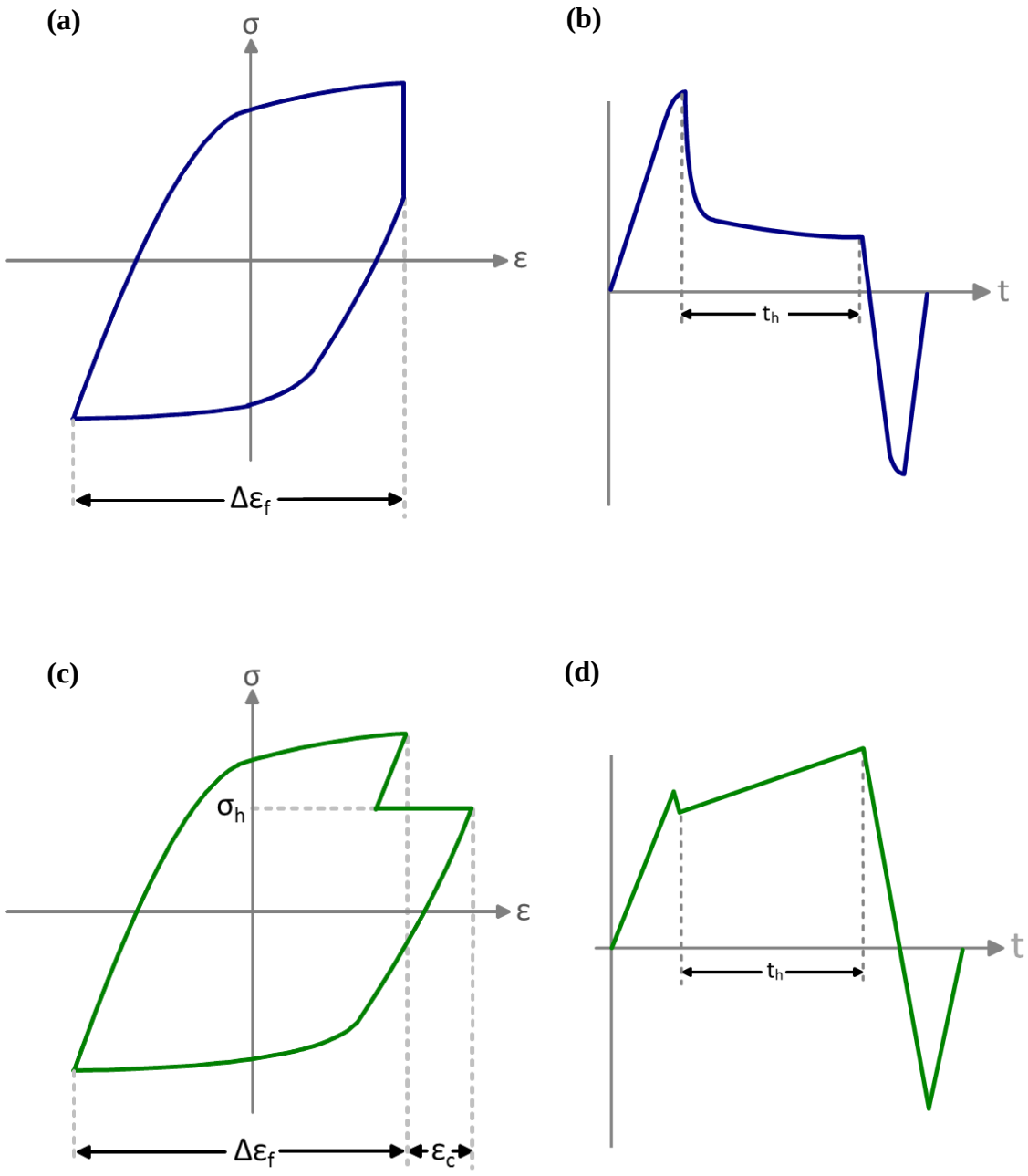

Fig. 4.1 (a), (b) – Traditional strain-controlled creep-fatigue loading profile; (c), (d) Hybrid-control loading profile.

In hybrid controlled tests, increasing the hold time causes a significant reduction in cycle life. This is contrary to strain controlled tests, where increasing the hold time beyond a certain threshold does not lead to any decrease in cycle life. The hybrid-control loading profile produces creep deformation instead of stress-relaxation during the hold period, thereby avoiding the saturation effect of increasing hold time on cycle life that is observed in strain-controlled testing. Moreover, in hybrid control loading profile, the stress at which creep occurs does not have to be the peak stress. Therefore, hybrid control loading waveforms can produce a variety of test data ranging from fatigue-dominated to creep-dominated interaction. In this study, the creep-fatigue interaction was varied by changing the fatigue strain range, (0.6% and 0.8%), holding stress (85 MPa and 100 MPa), and holding time (30 s, 180 s and 900 s). The 950°C creep-fatigue test data have been presented in [28]. Additional tests at 850°C were performed for this study. Fig. 4.2 shows the hysteresis curves, cyclic softening, and cyclic creep strain behavior for an 850°C test with 1.0% fatigue strain range, 100 MPa holding stress, and a 180s hold time. 850°C tests require longer hold periods than 950°C tests to produce the same amount of creep damage, as measured by effective time fraction approach. 850°C tests with hold periods of up to 10 hours were performed.

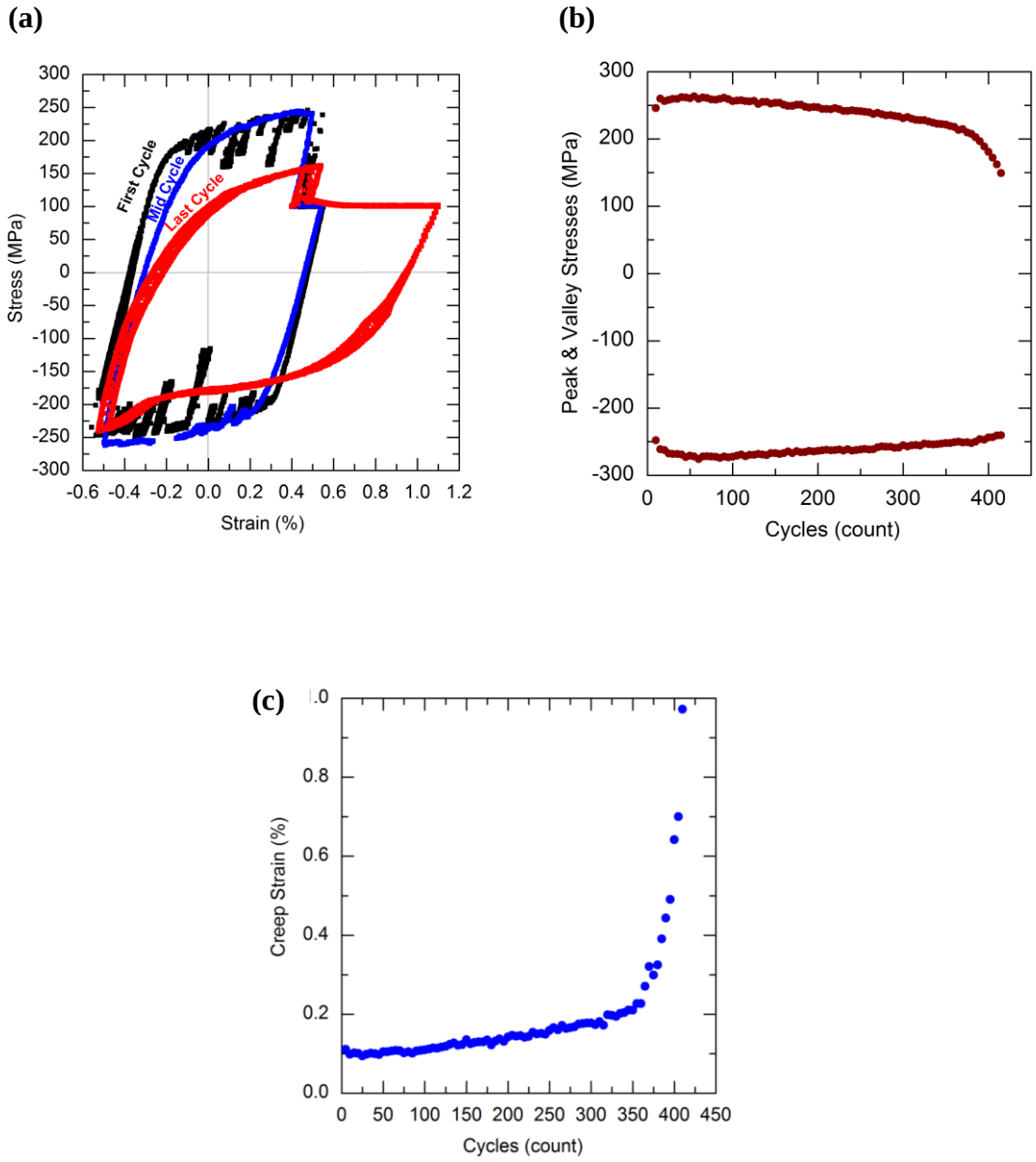

Fig. 4.2 – Test data from an 850°C test with 1.0% fatigue strain range, 100 MPa holding stress, and 180s hold time (a) Stress-strain curves from first, mid and last cycles and (b) Peak tensile and compressive stresses plotted against cycle count show cyclic softening; (c) Creep strain during the hold periods increases with cycles.

The new hybrid-controlled testing can produce data for creep dominated failure and is suitable for calibrating the entire damage interaction curve in the time fraction approach. Since the loading profile is very different from the classical strain-controlled testing, it was not clear how the micro-scale damage features related to the macro-level mechanical damage indicators (i.e., creep time fraction and fatigue cycle fraction). Thus, the authors performed an image-based analysis and statistical study to quantify the different micro-scale damage features of the failed specimens. Only the key results are shown here as they relate to the proposed life prediction model. Typical images for specimens with creep dominated failure and specimens with fatigue dominate failure are shown in Fig. 4.3(a) and Fig. 4.3(b), respectively. It was observed that creep dominated failure is characterized by a large number of internal voids and short and blunt surface cracks. On the contrary, fatigue dominated failure has minimal internal voids and long surface cracks. Thus, the internal void density and surface crack length are the representative micro-scale damage features for creep and fatigue, respectively. Extensive measurements were performed using a scanning electron microscope to quantify these two types of damage features for many different loading levels and hold periods. The quantified features were plotted against classical time fraction approach parameters to check for a correlation. The mean crack length vs. the fatigue damage fraction (i.e., n/N) is shown in Fig. 4.4(a). A good correlation was observed, suggesting that the fatigue cycle ratio is a reasonable indicator of fatigue damage. The void area fraction vs. the creep fraction in the classical time fraction approach (i.e., hold time/creep rupture time) is shown in Fig. 4.4(b). Different colors are used for different holding stress level and/or fatigue strain range. There is a poor correlation between void fraction and classical time fraction,

suggesting that the classical time fraction is not a reasonable indicator of creep damage. Thus, alternative mechanical parameters should be proposed and developed to better correlate with the micro-void density. The key challenge is how to define such a mechanical parameter and how to calculate this for arbitrary loading profiles for life prediction. This is the main motivation of the proposed study and is illustrated in detail in the next section.

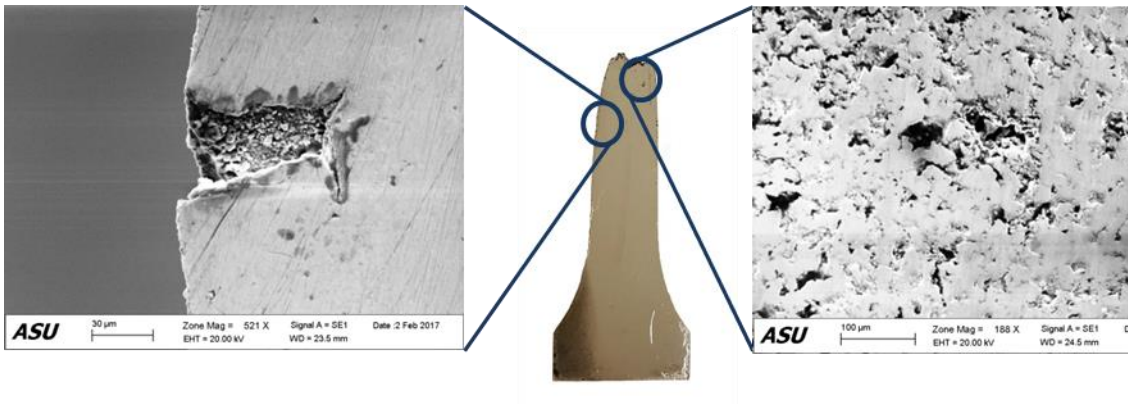

(a)

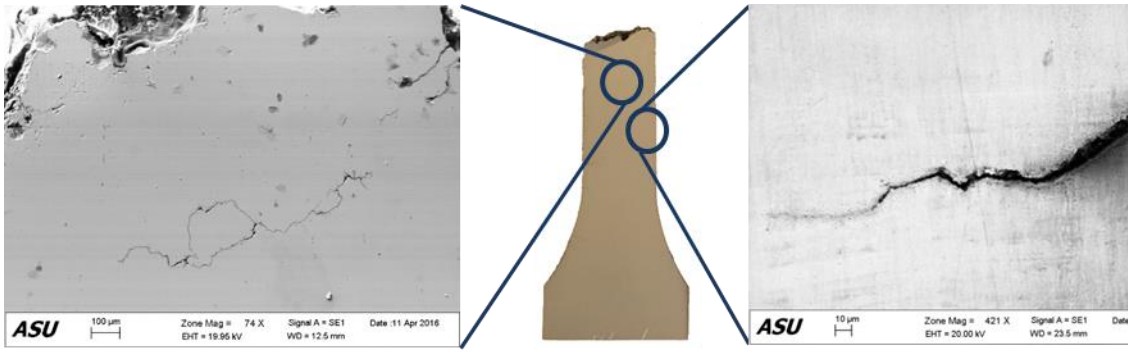

(b)

Fig. 4.3 (a) – Failed specimen with creep dominated failure shows short surface cracks and large internal voids and (b) – failed specimen with fatigue dominated failure shows minimal internal voids and long surface cracks.

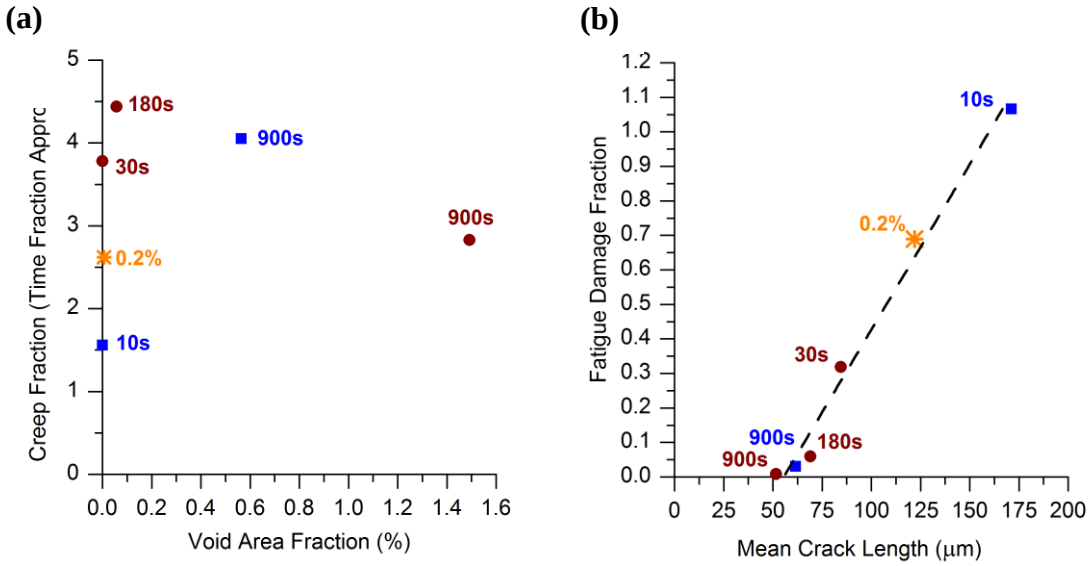

	Fatigue Strain Range (%)	Holding Stress (MPa)	Type of Hold Period
●	0.6	100	time limit
■	0.8	85	time limit
✱	0.8	85	strain limit

Fig. 4.4 (a) – Correlation between classical creep time fraction and area fraction of voids on the failed specimen; (b) – Correlation between fatigue cycle fraction and mean length of surface cracks on failed specimens.

4.3 PROPOSED LIFE PREDICTION MODEL

This section develops the proposed life prediction model. The classical time fraction approach is briefly reviewed, as it provides the basis for the proposed life prediction methodology. Following this, the basic hypothesis and derivation of the effective time fraction approach is shown based on the hybrid-controlled testing profile. Next, the model is extended to strain-controlled testing profile as well, which aims to unify the proposed concept to arbitrary loading waveforms. Details are shown below.

4.3.1 Review of the Time Fraction Rule

Linear summation of fatigue cycle fraction (D_f) and creep time fraction (D_c) in the classical time fraction approach can be stated as [22]:

$$\sum_i \left(\frac{N_{cf}}{N_f}\right)_i + \sum_j \left(\frac{t_h}{T_r}\right)_j \leq D \qquad (1)$$

where, N_{cf} is the cycle life in the creep-fatigue testing, N_f is the cycle life in pure fatigue testing at the same strain level, t_h is the tensile hold time, T_r is time to rupture in pure creep testing. D is a material dependent parameter. Creep-fatigue interaction is known to follow a bilinear trend line on a damage interaction diagram for some steels [21,30,39].

In the case of Alloy 617 at 800-1000˚C, use of the time fraction rule to calculate creep damage results in large scatter and absence of a trend on the creep-fatigue interaction diagram [5,9,39]. There are several reasons for the absence of a trend on the interaction diagram: (i) Rapid stress relaxation of Alloy 617 at high temperatures means that increasing the hold time does not necessarily lead to a decrease in cycle life. After the initial phase of rapid stress relaxation, maintaining the strain hold for a longer period of time does not lead to an increase in creep strain. This is also known as the saturation effect of hold time on creep damage [7]; (ii) The time fraction rule assumes that the entire hold time is involved in irreversible creep deformation. For this to be true, the creep time fraction cannot be larger than unity [13]. On the contrary, creep fractions larger than unity have been reported for several metals [5,14,21,22,31,35]; (iii) Creep-fatigue tests are traditionally conducted in strain-control where there is stress relaxation during the hold time, instead of creep deformation. The creep time fraction, in which hold time is

normalized by creep rupture time, then assumes that steady-state creep behavior and stress relaxation response are mechanistically equivalent.

4.3.2 Effective Time Fraction Approach – Hybrid-Controlled Testing

As illustrated in the previous section, image analysis shows that the classical time fraction parameter for calculation for creep damage does not show a good correlation with the micro-scale damage features. Further evidence for this hypothesis is obtained when the experimental data are plotted on a damage diagram using the classical time fraction approach. This damage diagram is shown in Fig. 4.5. The data shows a large scatter with most of the creep fractions exceeding unity. This confirms that the classical time fraction approach is not appropriate for the creep-fatigue life prediction, at least for the hybrid-controlled testing data. The creep damage fraction should, in principle, be less than unity for the creep-fatigue testing with an extreme value of unity being achieved for pure creep rupture testing. This observation indicates that the classical time fraction calculation for creep damage 'overestimates' the creep damage by using the entire duration of the hold time. In other words, only a portion of the hold time contributes to the creep damage so the calculation of the creep damage should only count this 'effective' portion of the hold time. For this reason, the proposed approach is called the effective time fraction approach.

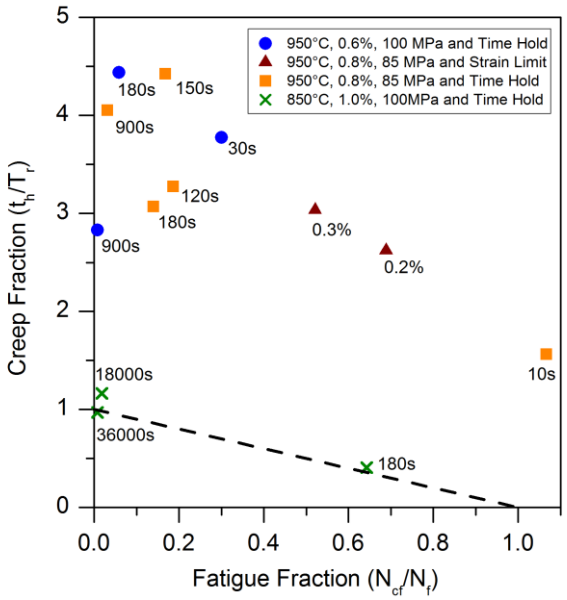

Fig. 4.5 – Damage interaction diagram using time fraction rule for hybrid-controlled creep-fatigue tests.

A hypothesis is proposed based on the above observations: the effective hold time corresponds to the time spent for the net creep strain increment compared to the last cycle. In hybrid-controlled testing, cyclic softening is observed and the creep strain rate during the hold time increases with cycles. The effective time fraction approach assumes that after the first cycle, only a fraction of the hold time is involved in the net creep deformation. This fraction, called effective hold time (t_{eh}), is part of the hold time during which a net increase of creep strain occurs with respect to the previous cycle. The schematic in Fig. 4.6 shows the application of the effective time fraction approach to the first three cycles of a creep-fatigue test with fixed hold time per cycle. Given that hold time is fixed, effective hold time for each cycle is the time spent to increase the creep

strain from the creep strain in the previous cycle. It can be calculated by considering the increase in creep strain rate with each cycle as:

$$\sum t_{eh} = \sum_{k=0}^{N_{cf}-1} \left(\frac{\dot{\varepsilon}_{k+1} - \dot{\varepsilon}_k}{\dot{\varepsilon}_{k+1}}\right)\left(t_{h(k+1)}\right) \tag{2}$$

where, $\dot{\varepsilon}_k$ represents the creep strain rate in cycle number *k*. The linear summation of creep and fatigue damage then becomes:

$$\sum_i \left(\frac{N_{cf}}{N_f}\right)_i + \sum_j \left(\frac{t_{eh}}{T_r}\right)_j \leq D \tag{3}$$

where, the first term is the fatigue damage fraction and the second term is the effective creep damage fraction.

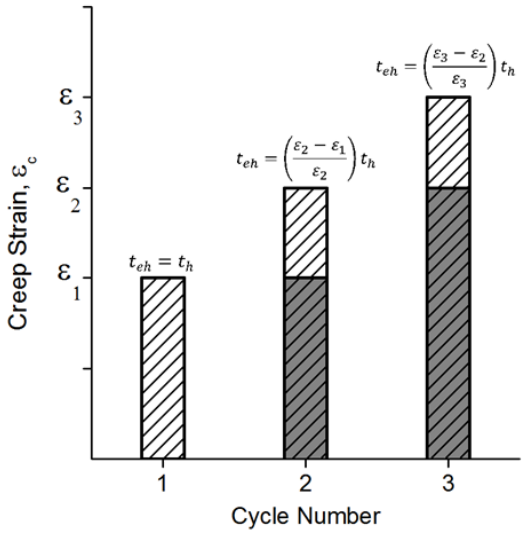

Fig. 4.6 – Schematic showing first three cycles of a creep-fatigue test. White shaded area represents the strain accumulated during the effective hold time.

For tests with fixed hold time per cycle, Eq. (2) can be simplified as:

$$\sum t_{eh} = t_h \left(\sum_{k=0}^{n-1} \left(\frac{\varepsilon_{(k+1)} - \varepsilon_{(k)}}{\varepsilon_{(k+1)}} \right) \right) \tag{4}$$

Similarly, for tests with fixed creep strain per cycle, Eq. (2) can be simplified as:

$$\sum t_{eh} = \sum_{k=0}^{n-1} \left| t_{h(k)} - t_{h(k+1)} \right| \left(\frac{t_{h(k+1)}}{t_{h(k)}} \right) \tag{5}$$

In hybrid-control tests, the stress is constant during the hold time so the effective creep damage fraction (D_{ec}) is:

$$D_{ec} = \frac{\sum_{k=1}^{N_{cf}} (t_{eh})}{T_r} \tag{6}$$

The inputs required for this calculation are: creep strain rate/creep strain as a function of cycles, and creep rupture time. For tests with fixed hold time per cycle, the creep strain (ε_c) is approximated as:

$$\varepsilon_c = c_1 e^{c_2 (\frac{k}{N_{cf}})} \tag{7}$$

where, $c_1$and c_2 are fitting constants for the creep strain vs normalized cycles curve. An average curve between creep strain rate and normalized cycles is shown in Fig. 4.7 for multiple hybrid-control tests. Substituting Eq. (7) into Eq. (4) and simplifying gives:

$$\sum_{k=1}^{N_{cf}} t_{eh} = N_{cf}\left(1 - e^{-\frac{c_2}{N_{cf}}}\right) \tag{8}$$

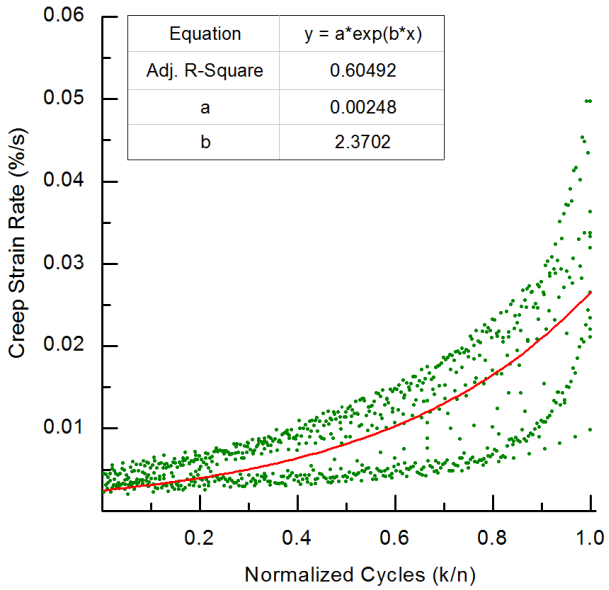

Fig. 4.7 – Exponential relation between creep strain rate and normalized cycles. Green dots represent creep strain rate vs cycles data from multiple hybrid-control

Thus, for hybrid-control tests with a fixed hold time per cycle, the linear damage summation rule of Eq. (1) becomes:

$$\sum_i \left(\frac{N_{cf}}{N_f}\right)_i + \sum_j \left(\frac{N_{cf}\left(1 - e^{-\frac{c_2}{N_{cf}}}\right)}{T_r}\right)_j \leq D \tag{9}$$

where, N_{cf} is the unknown. N_f is from the fatigue strain-life curve. T_r is the creep rupture time from the creep Larson-Miller plot. c_2 is from the creep strain vs normalized cycles curve fit and D is from the creep-fatigue interaction diagram for the given material and temperature.

4.3.3 Effective Time Fraction Approach – Strain-Controlled Testing

This section extends the effective hold time concept to the classical strain-controlled test using literature test data. The hybrid-control loading profile has a force-controlled hold period so the net creep increment can be extracted directly from the hysteresis curve. However, for strain-controlled tests, which have stress relaxation during the hold period, the net creep increment per cycle must be calculated. In the strain-controlled tests, the stress relaxation data can be fitted by [30]:

$$\sigma = \frac{\sigma_0(N)}{e^{b_1 t^{b_2}}} \tag{10}$$

where, $\sigma_0(N)$ is the peak stress for cycle N. t is the time from start of the hold period. b_1 and b_2 are fitting constants for the stress relaxation curve. The peak stress drops as a function of cycles due to the cyclic softening and damage accumulation. In the proposed study, it is approximated as:

$$\sigma_0(N) = a_1 N^4 + a_2 N^3 + a_3 N^2 + a_4 N + a_5 \tag{11}$$

where, a_{1-5} are fitting constants. Total strain (ε_t), which is constant for each cycle, can be decomposed as:

$$\varepsilon_t = \varepsilon_e + \varepsilon_p + \varepsilon_c \tag{12}$$

where, $\varepsilon_e$is the tensile elastic strain. ε_p is the tensile plastic strain. ε_c is the creep strain. Rearranging Eq. (12) and substituting Eq. (10):

$$\varepsilon_c = \varepsilon_t - \varepsilon_p - \frac{\sigma_0(N)}{Ee^{b_1 t^{b_2}}} \tag{13}$$

For Cycle 1:

$$t' = 0 \tag{14}$$

$$t_{eh}(N=1) = t_h - t' = t_h \tag{15}$$

$$\varepsilon_c(t = t_h, N = 1) = \varepsilon_t - \varepsilon_p - \frac{\sigma_0(1)}{Ee^{b_1 {t_h}^{b_2}}} \tag{16}$$

where, t' is defined as the time in current cycle when the creep strain equals the creep strain in the previous cycle.

For Cycle 2:

At $t = t'$, the creep strain in current cycle equals the creep strain in previous cycle, i.e.

$$\varepsilon_c(t', 2) = \varepsilon_c(t_h, 1) \tag{17}$$

$$\varepsilon_t - \varepsilon_p - \frac{\sigma_0(2)}{Ee^{b_1 {t'}^{b_2}}} = \varepsilon_t - \varepsilon_p - \frac{\sigma_0(1)}{Ee^{b_1 {t_h}^{b_2}}} \tag{18}$$

Assuming that the plastic strain and Young's modulus do not change significantly for consecutive cycles, Eq (18) becomes:

$$\ln\left(\frac{e^{b_1 {t_h}^{b_2}}}{e^{b_1 {t'}^{b_2}}}\right) = \ln\left(\frac{\sigma_0(1)}{\sigma_0(2)}\right) \tag{19}$$

$$b_1 {t_h}^{b_2} - b_1 {t'}^{b_2} = \ln\left(\frac{\sigma_0(1)}{\sigma_0(2)}\right) \tag{20}$$

$$t' = \left[{t_h}^{b_2} - \frac{1}{b_1}\ln\left(\frac{\sigma_0(1)}{\sigma_0(2)}\right)\right]^{1/b_2} \tag{21}$$

Therefore, for Cycle N:

$$t'(N) = \left[\left(t'(N-1)\right)^{b_2} - \frac{1}{b_1}\ln\left(\frac{\sigma_0(N-1)}{\sigma_0(N)}\right)\right]^{1/b_2} \tag{22}$$

Effective creep damage fraction for the strain-controlled test is given by:

$$D_{ec} = \sum_{N=1}^{N_{cf}} \int_{t'(N)}^{t_h} \left(\frac{1}{T_r}\right) dt \tag{23}$$

Similar to the last section for the hybrid-controlled test, Eq. (23) and Eq. (3) provide the proposed life prediction for a strain-controlled test.

4.4 RESULTS AND DISCUSSION

This section demonstrates the application and validation of the proposed life prediction model to Alloy 617 at high temperatures. The model was first validated using the 950°C test data. Two types of data was used. The first type is the hybrid-controlled testing data reported in [28]. For each strain range (i.e. 0.6% and 0.8%), the hybrid-controlled tests used holding stresses of 85MPa or 100MPa and various hold times. The second type is strain-controlled test data reported in [29]. For each strain range (i.e. 0.3%, 0.6%, and 1.0%), the strain-controlled tests had hold times of 180s, 600s, or 1800s. The effective time fraction approach is used to plot the experimental data in Fig. 4.8. The x-axis is the fatigue cycle fraction and the y-axis is the effective time fraction for creep damage. A clear bilinear trend is observed and experimental data has considerably less scatter compared to the plot that used classical time fraction approach.

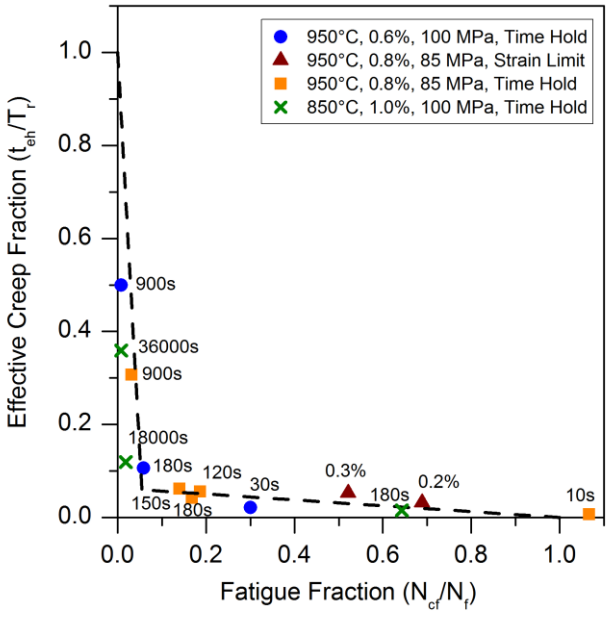

Fig. 4.8 – Damage interaction diagram using effective time fraction approach for hybrid-controlled creep-fatigue tests.

An intersection point of (D_f, D_{ec}) = (0.0542, 0.0595) was obtained by curve fitting the 950°C hybrid-controlled test data, as shown in Fig. 4.9(a). ASME draft code case for Alloy 617, which uses the classical time fraction rule, suggests (D_f, D_c) = (0.1, 0.1) as the intersection point for the bilinear damage envelope [9]. The values of the effective creep fraction were less than 0.005 for all strain-controlled tests, indicating minimal creep damage. The implication that strain-controlled tests are not capable of generating significant creep damage is supported by damage observations of failed test specimens, which only show intergranular fatigue cracks and no creep voids [8]. The life-prediction for all tests is shown in Fig. 4.9(b). The x-axis is the experimental observed life and the y-axis the predicted life using the effective time fraction model. Most data fall into the scatter band with a life factor of 3. It should be noted that there is a systematic error associated with the strain-controlled testing data as all predicted lives are longer than the experimental lives. The reason for this behavior is not clear for now. The authors suspected that this is possibly due to additional damage mechanisms that exist in the strain-controlled CF testing, which are not included in the current formulation. Additional experimental and theoretical investigation is required to further explain this observation.

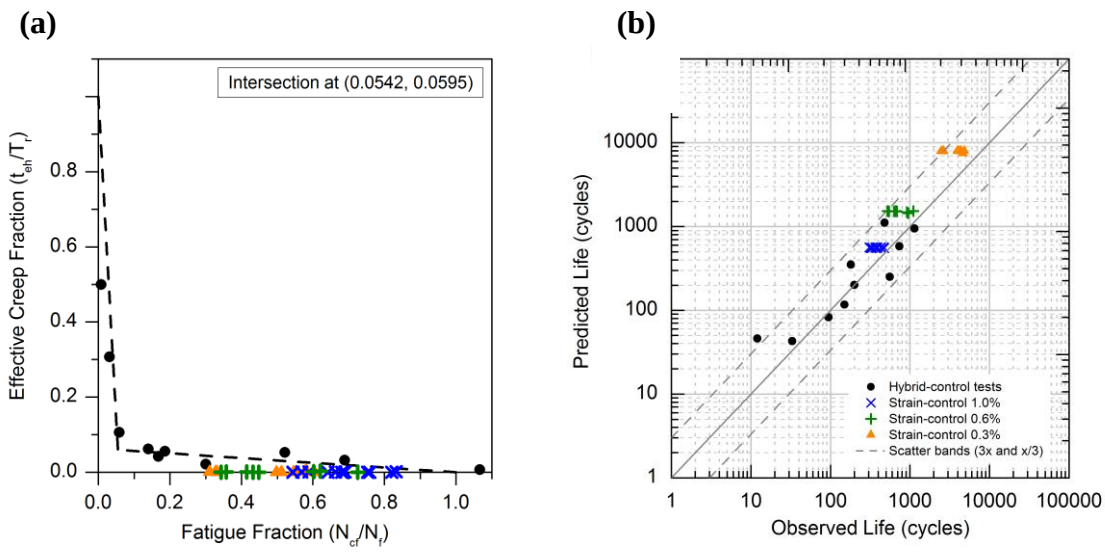

Fig. 4.9 – (a) Creep-fatigue interaction diagram and (b) life prediction using effective time fraction approach for strain-control [29] and hybrid-control tests at 950°C.

Additional hybrid-control tests were performed at 850°C to check the existence of a bilinear interaction trend as well as the applicability of the proposed life prediction model. Fig. 4.10(a) shows the bilinear trend at 850°C. In comparison to the 950°C data, the intersection point for 850°C data is closer to the origin of the interaction diagram. Fig. 4.10(b) shows again that the life-prediction for these tests also lies within a scatter band of 3. Due to the limited number of specimens available for testing at this temperature, only four data points are reported for the holding stress of 100 MPa with varying holding periods. Additional experiments at other holding stresses may be required for a more comprehensive evaluation.

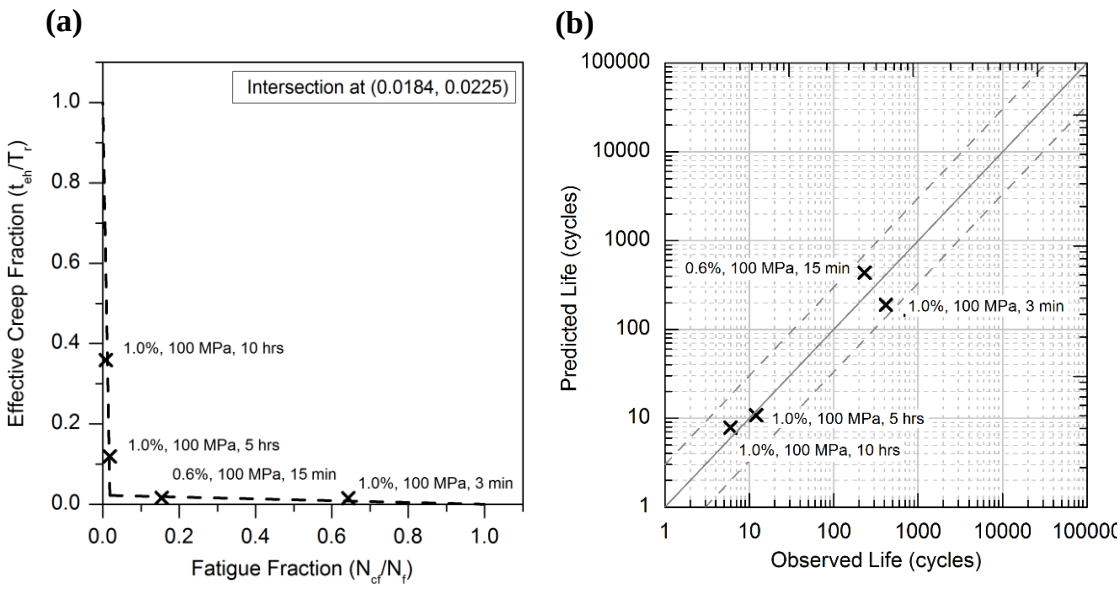

Fig. 4.10 – (a) Creep-fatigue interaction diagram with data labels indicating fatigue strain range, holding stress, and hold time; (b) life prediction using effective time fraction approach for hybrid-control tests at 850°C.

Physical evidence for the effective time fraction approach is provided by Fig. 4.11, where a correlation can be seen between effective time fraction for creep and the area fraction of voids on failed 950°C test specimens. Unlike the classical time fraction approach shown in Fig. 4.5, Fig. 4.11 shows that a larger effective creep fraction corresponds to larger void area fraction.

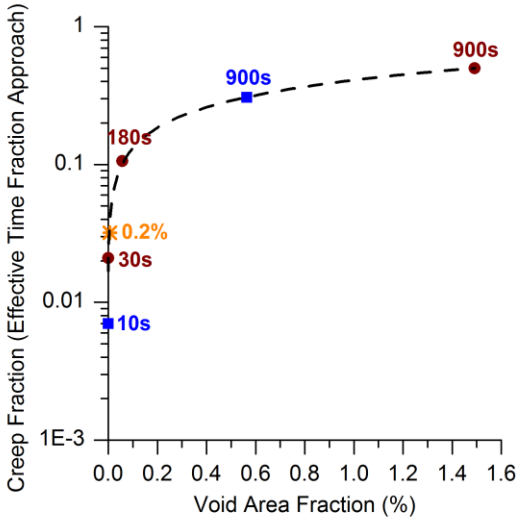

	Fatigue Strain Range (%)	Holding Stress (MPa)	Type of Hold Period
●	0.6	100	time limit
■	0.8	85	time limit
✱	0.8	85	strain limit

Fig. 4.11 – Correlation between effective time fraction for creep and area fraction of voids on the failed specimen;

4.5 CONCLUSION

An effective time fraction approach, that considers the increase in creep strain with cycles, is introduced within the framework of the widely-used time fraction and damage summation rule. Several major conclusions can be drawn based on this study.

- Classical time fraction rule fails to correlate with the hybrid-controlled creep-fatigue test data and the creep fraction is usually larger than unity, which is not physically sound;

- The effective time fraction approach correlates well with experimental data with smaller scatter bands in life prediction;
- The damage diagram using the effective time fraction concept has a clear bilinear trend for the experimental data;
- A lower temperature will move the intersection point of the bilinear curve (in the effective time fraction approach) towards the origin of the damage interaction diagram.
- The proposed model shows a systematic error for strain-controlled testing although the scatter band is less than 3.

The proposed model relies on the hypothesis that only the time during the net creep strain increment is responsible for the creep damage. This is only tested for Alloy 617 at temperatures of 850°C and 950°C. Extension of this concept to other materials at high temperatures needs significant future research. Care must be taken when using the conclusions of this study to lower temperatures as the deformation mechanisms are different and stress relaxation behavior may not be as significant as Alloy 617 at high temperatures. Additional study is required to investigate the proposed model to strain-controlled experiments as the results suggest additional failure mechanisms may exist. The proposed model is a phenomenological model that is supported by observations of physical damage. Approaches based on damage mechanics and fracture mechanics may provide more physical insights into life prediction of hybrid-controlled and strain-controlled test data.

5. UNIFIED VISCOPLASTICITY MODELING FOR CREEP-FATIGUE LIFE PREDICTION

5.1 INTRODUCTION

Design codes for nuclear components typically adopt simple empirical models such as time fraction rule [32,41], ductility exhaustion [33], and strain range partitioning [36] to evaluate creep-fatigue life. The life assessment rules are calibrated by fitting experimental data from many creep-fatigue tests. Running elevated temperature tests is time consuming and resource intensive. Moreover, the loading waveforms for such tests are not fully representative of the actual operating conditions of the components. Reliable life prediction for components under complex loading waveforms can be achieved by modeling the constitutive behavior of the material as well as the effects of microstructural damage. The stresses and strain rates during service conditions of the components are lower than what can be realistically achieved in creep-fatigue tests. Constitutive modeling of cyclic deformation provides a means for extrapolating the results of short-term tests to long-term operating conditions of the components.

Viscoplastic models are rate-dependent and therefore suitable for modeling the cyclic deformation of metals and alloys at elevated temperatures. The Chaboche unified viscoplastic model is used in literature to model a wide variety of materials [42–44], including Ni-base superalloys at elevated temperatures [45–50]. Carroll et al. [51] demonstrated the capability of the Chaboche model to simulate the creep-fatigue response of Alloy 617 at 850 and 950°C. Sham et al. [52] used the Chaboche model to simulate low-stress long-term creep behavior of Alloy 617. This model employs

mechanism-based internal state variables to capture various features of the stress-strain response including monotonic hardening, cyclic hardening and softening, Bauschinger effect and partially ratchetting [53]. The unified viscoplastic model makes use of internal state variables, e.g. back stress and drag stress [54], that are analogous to physical deformation mechanisms[55]. The back stress variable represents the interaction of moving dislocations with grain boundaries, whereas the drag stress variable represents the interaction of moving dislocations with precipitates or solute atoms. Since, plasticity and creep are governed by the same deformation mechanism i.e. movement of dislocations, the unified viscoplastic model represents the plastic and creep strains by a single variable known as inelastic strain.

In Alloy 617, creep damage is produced by nucleation and linkage of intergranular voids, whereas fatigue damage is caused by initiation and growth of oxidation-induced surface cracks [25,26,40,56–58]. The interaction between creep and fatigue damage mechanisms accelerates failure under creep-fatigue conditions. The effects of microscopic damage are incorporated into the macroscopic unified viscoplastic model with the introduction of internal damage variables [44,59–61]. Typically, the creep damage variable is a function of time and fatigue damage variable is a function of cycles. The simultaneous effect of creep and fatigue is modeled by linear or non-linear accumulation of creep and fatigue damage variables [44].

This study combines the unified viscoplastic model with a damage variable based on a model parameter to predict creep-fatigue life of Alloy 617 at 950°C for a non-standard loading waveform with strain-controlled ramps and force-controlled tensile hold periods.

First, the details of the internal variables including model equations are provided. Following this, the optimization of model parameters and sensitivity of the model to changes in these parameters are discussed. Next, damage evolution equations based on the results of sensitivity analysis are introduced along with a damage interaction model based on creep and fatigue energy. The damage model is calibrated using creep-fatigue tests. Finally, life prediction results for creep-fatigue tests are compared with experimental data.

5.2 RESULTS AND DISCUSSION

5.2.1 Unified Viscoplastic Model

The uniaxial form of the unified viscoplastic model used in this study is adopted from Chaboche and Rousselier [42,62]. The total strain, ε, is decomposed into elastic, ε^e, and inelastic, ε^{in}, parts:

$$\varepsilon = \varepsilon^e + \varepsilon^{in} \tag{1}$$

The flow rule relates the inelastic strain rate, $\dot{\varepsilon}^{in}$, to the stress, σ, and internal variables i.e. back stress, χ, and drag stress, *R*.

$$\dot{\varepsilon}^{in} = \langle {}^{f}/_{Z} \rangle^n \, sgn(\sigma - \chi) \tag{2}$$

where,

$$sgn(x) = \begin{cases} 1, & x > 0 \\ 0, & x = 0 \\ -1, & x < 0 \end{cases} \qquad \text{and} \qquad \langle x \rangle = \begin{cases} x, & x \geq 0 \\ 0, & x < 0 \end{cases}$$

Consequently, the viscoplastic multiplier, $\dot{p}$, is defined as

$$\dot{p} = \left\langle \frac{f}{Z} \right\rangle^{n} \tag{3}$$

where, Z and n are viscous parameters responsible for rate dependence of the stress. The function, f, defines the elastic domain as

$$f(\sigma, \chi, R) = |\sigma - \chi| - R - \sigma_{Y0} \leq 0 \tag{4}$$

where, σ_{Y0} is the initial yield stress.

The back stress, χ_i , controls the direction-dependent Bauschinger effect. The evolution of the back stress follows the non-linear kinematic hardening rule of Armstrong and Frederick [63].

$$\dot{\chi}_i = C_i\left(a_i \dot{\varepsilon}^{in} - \chi_i \dot{p}\right) \tag{5}$$

where, C_i and a_i are constants, and i = 1, 2

The drag stress, R, controls the direction-independent cyclic hardening or softening, also known as isotropic hardening. The drag stress evolves as

$$\dot{R} = b(Q - R)\dot{p} \tag{6}$$

where, b and Q are constants.

The viscous overstress, $\dot{\sigma}_v$, is given by the Norton's power law equation for steady-state creep

$$\sigma_v = Z\dot{p}^{1/m} \tag{7}$$

The stress decomposition is as follows

$$\sigma = \chi + (R + \sigma_{Y0} + \sigma_v)sgn(\sigma - \chi) \tag{8}$$
$$= E(\varepsilon - \varepsilon^{in})$$

This form of the model requires 10 material parameters, namely, the Young's modulus, *E*; kinematic hardening parameters, a_1, a_2, C_1, C_2; isotropic hardening parameters, *b* and *Q*; viscous parameters, *Z* and *m*; and the initial yield stress, σ_{Y0}.

5.2.2 Calibration of Model Parameters

The system of ordinary differential equations from the unified viscoplastic model was solved in Matlab using the 'ODE45' solver which uses an explicit Runge-Kutta method. The parameters were then optimized relative to an experimental stress-strain curve, using the 'fminsearch' function in Matlab. The strain-controlled loading and unloading parts were optimized first by comparing the stresses. Subsequently, the stress-controlled tensile hold period was optimized by comparing the strains. Initial estimates for the material parameters were taken from [64]. Table 5.1. shows the initial and optimized model parameters.

	E (GPa)	**σ_{y0} (MPa)**	**b**	**Q (MPa)**	**a_1 (MPa)**	**C_1**	**a_2 (MPa)**	**C_2**	**Z (MPa $s^{1/m}$)**	**m**
Initial parameters	139	30	28.6	27.4	80	7112	116	929	170	10
Optimized parameters	124	19.4	43.7	-43.9	-394	1650	700	1583	706	3.69

Table 5.1. Initial and optimized model parameters for Alloy 617 at 950°C

5.2.3 Damage Model

The hybrid-control creep-fatigue loading waveform is particularly suitable of generating varying proportions of creep and fatigue damage. Unlike the traditional strain-controlled creep-fatigue loading, where strain hold periods cause stress relaxation, the hybrid-control loading profile employs stress-controlled hold periods to generate creep deformation. Under such loading conditions, the two main indicators of damage are: (i) the decrease in peak stress with cycles; and (ii) the increase in creep strain with cycles. Therefore, the sensitivity of these indicators to changes in model parameters were analyzed. Since, the strain range for the fatigue cycle is fixed, the changes in creep strain can be represented by peak strain. Fig. 5.1(a) and (b) show a sensitivity analyses for peak stress and peak strain respectively, for a single cycle by changing one model parameter at time.

The sensitivity analysis shows that both peak stress and peak strain are most sensitive to the viscous parameter, ‘m’. Additionally, reducing ‘m’ can simultaneously cause a drop in peak stress and a rise in creep strain. Although the model is also sensitive to parameters Z, a_1, and a_2; the parameter ‘m’ is selected to represent the damage due to its physical importance as the power in the Norton law equation, which relates applied stress to the secondary creep strain rate.

(a)

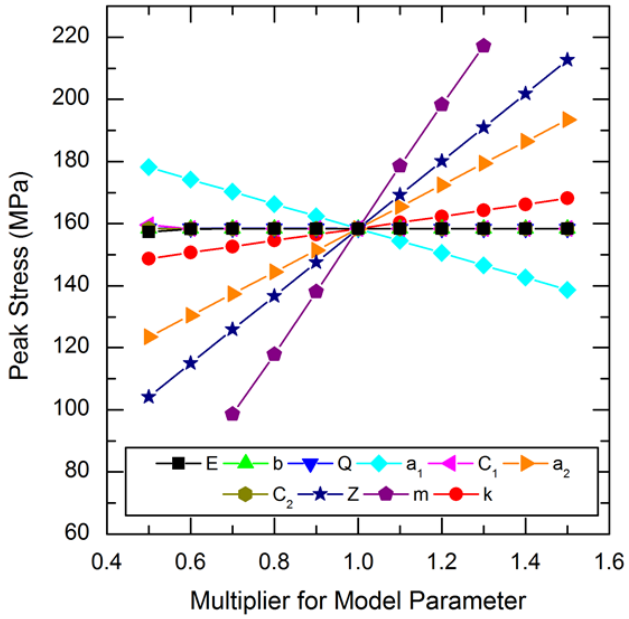

(b)

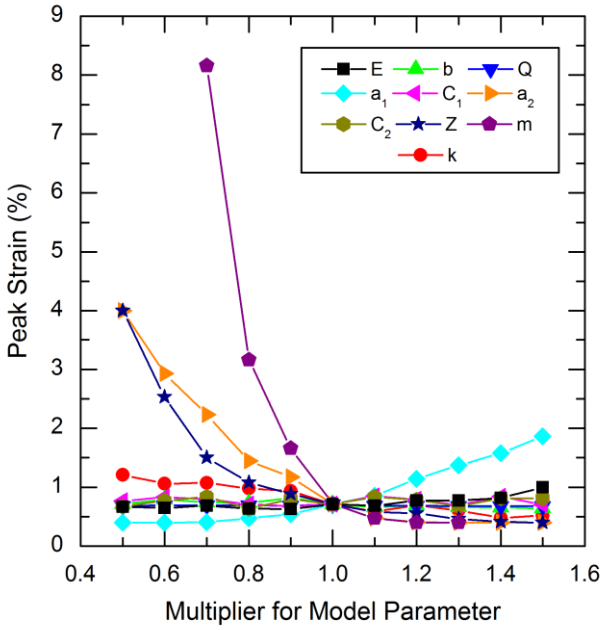

Fig. 5.1 – Sensitivity of (a) peak stress and (b) peak strain to changes in model parameters.

Next, the experimental hysteresis data from a hybrid-control creep-fatigue test was combined with the sensitivity analysis results to obtain the degradation of Young's modulus, E, and viscous parameter, m, as decreasing functions of cycles, n. The model equations were then solved in Matlab to find the accumulated fatigue energy, ΣE_f, and cyclic creep energy, E_c. The model was then fitted with creep-fatigue data from multiple tests to find a creep-fatigue interaction relation (Eq. 9) when equivalent damage, D_{eq}, equals unity. Fig. 5.2 shows the result of this fitting.

$$D_{eq} = \left(\frac{\sum E_f}{\sum E_f^*}\right)^q + \left(\frac{E_c}{E_c^*}\right)^q = 1 \qquad (9)$$

Following this, the degradation of parameter 'm' in the simulation with damage function, D_{eq}, was found. Fig. 5.3 show this degradation. Fig. 5.4 shows the procedure followed for calibrating the damage model for parameter 'm'. A similar procedure was followed for Young's modulus, E. ΣE_f^* is the accumulated fatigue energy for a pure fatigue test and E_c^* is the creep energy from a pure creep test.

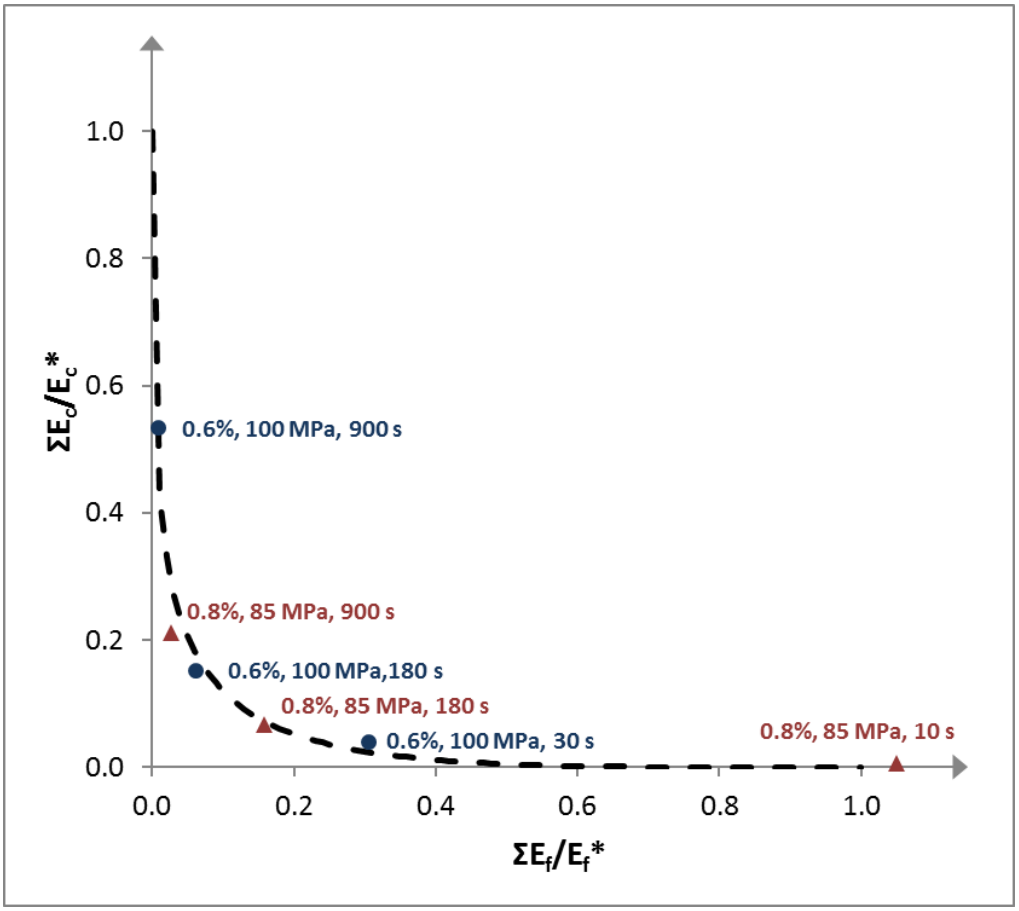

Fig.5.2 – Damage interaction diagram to determine the exponent 'q' in damage interaction rule.

(a)

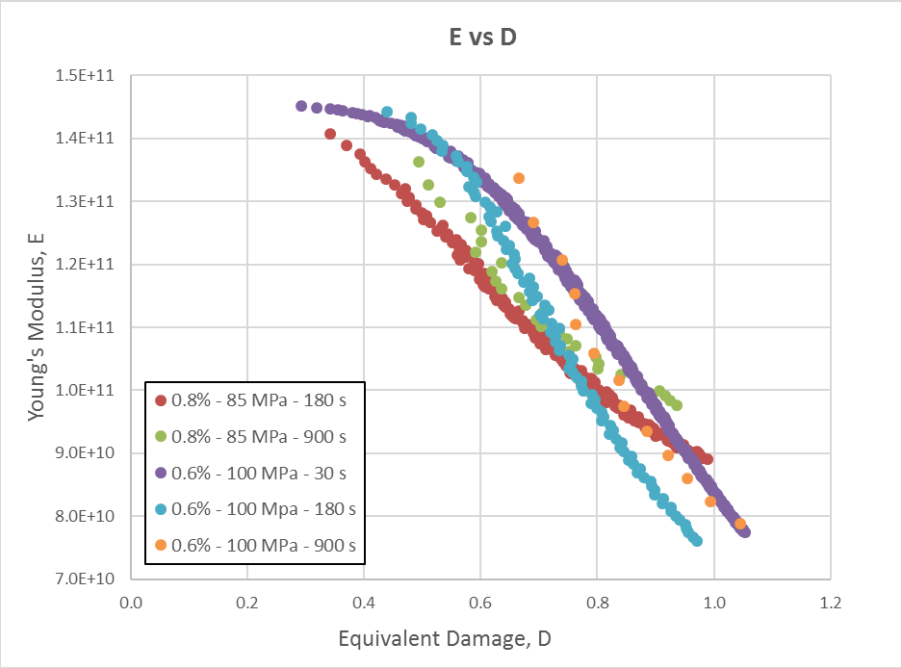

(b)

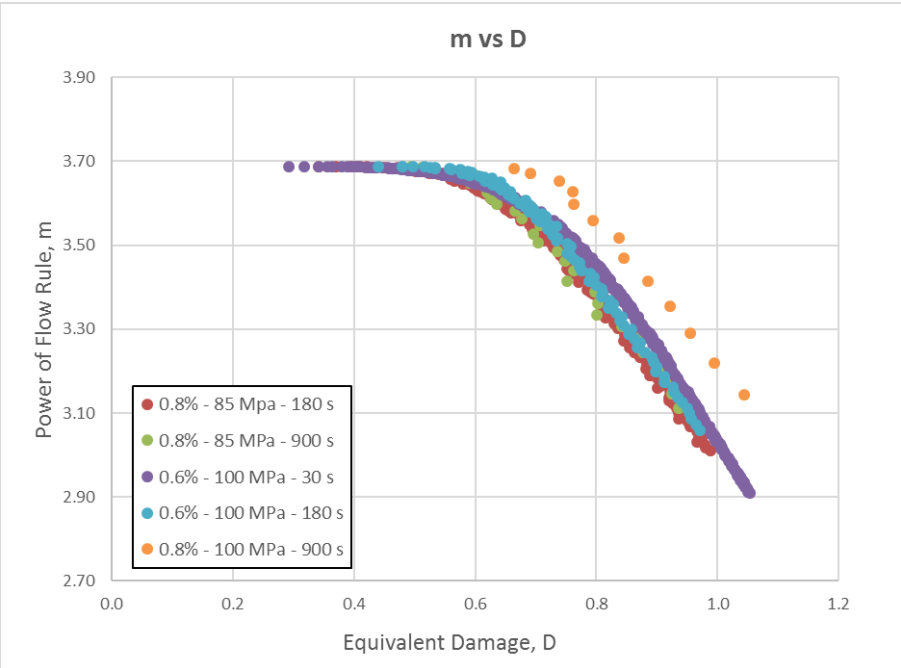

Fig. 5.3 – Degradation of model parameters (a)'m' and (b)'E' with equivalent damage, D_{eq} for multiple tests

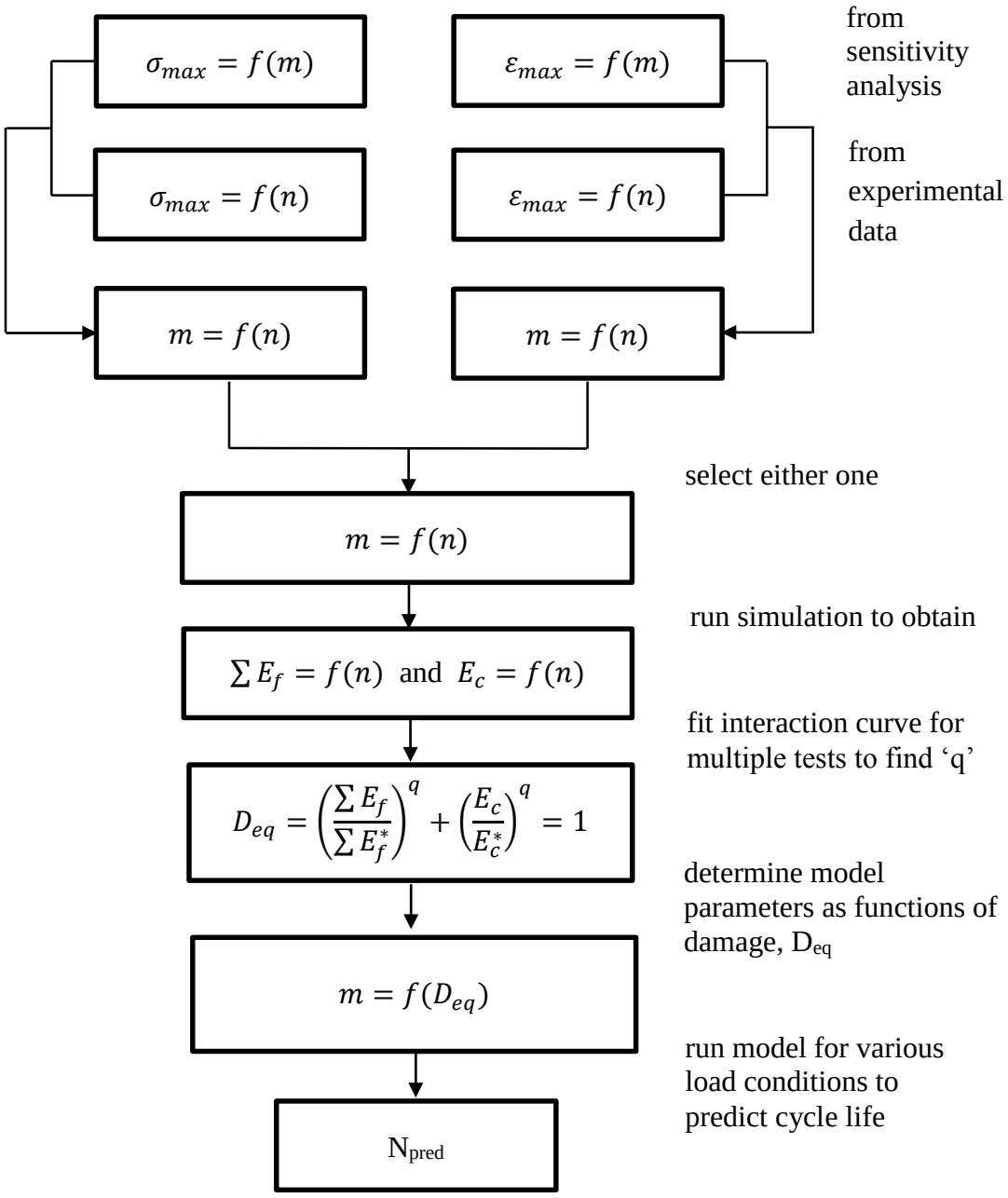

Fig. 5.4– A flowchart showing the development of the life-prediction rule for parameter 'm', from the experimental data and damage law.

5.2.4 Life Prediction and Model Validation

Fig. 5.5 shows the final life-prediction for the tests. Predicted lives fall within a scatter band of 2. This is better than the effective time fraction approach.

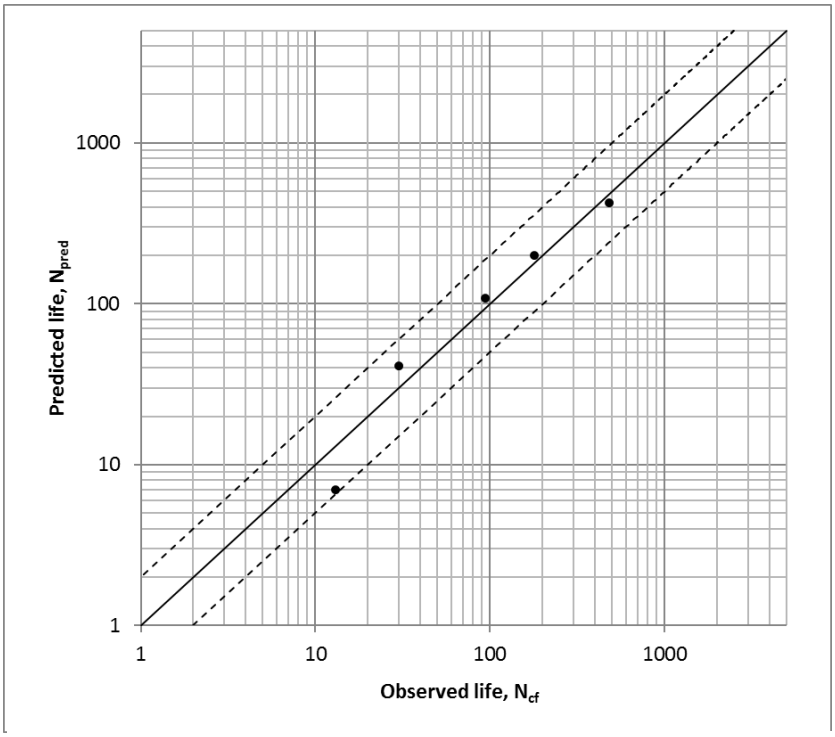

Fig. 5.5 – Predicted vs observed cycle for hybrid-control tests.

The viscoplastic model with damage was finally run to compare the stress-strain response, cyclic softening, and creep strain increase with experimental data. Fig. 5.6 shows the stress-strain curves for experiment and simulation for cycle 10, mid cycle and last cycle of a hybrid-control test with 0.8% strain range, 85 MPa holding stress, and a 180 s hold time. Fig. 5.7 shows the cyclic softening and peak strain increase behavior comparison.

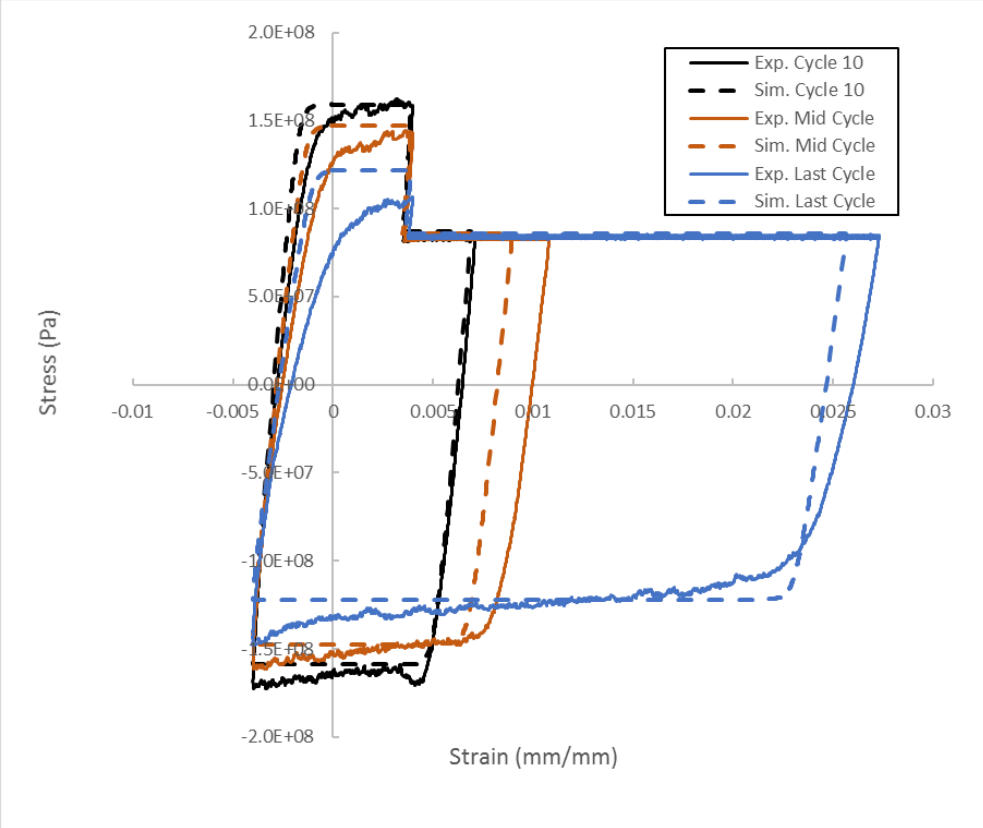

Fig. 5.6 – Stress-strain response for various cycles compared with experiment for a hybrid control test with 0.8% strain range, 85 MPa holding stress, and 180 s hold

(a)

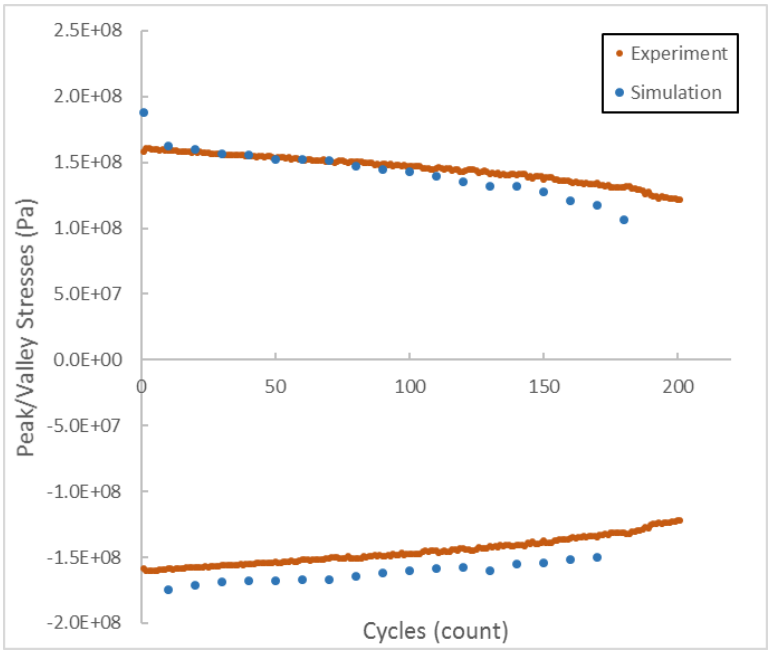

(b)

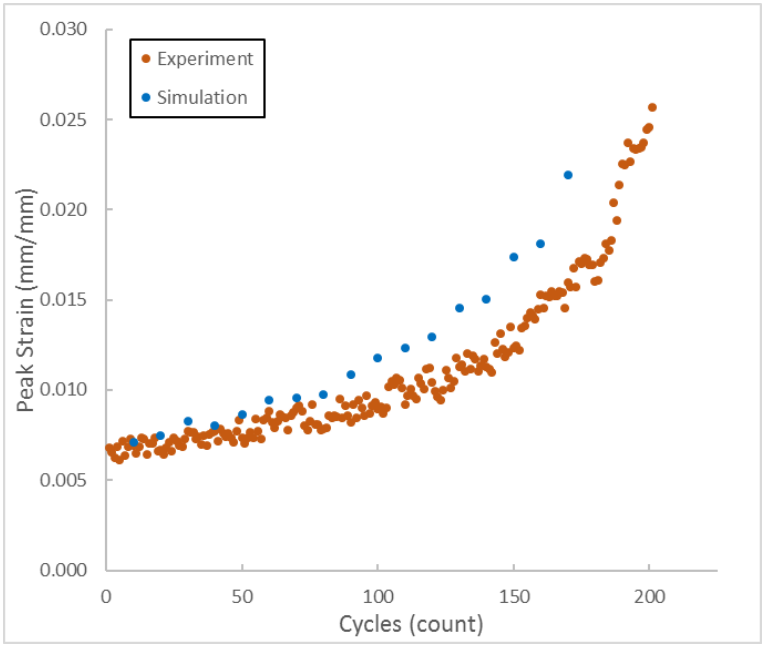

Fig. 5.7 – (a) Cyclic softening and (b) peak strain increase comparison between experiment and simulation.

5.3 CONCLUSION

A unified viscoplastic model is coupled with a non-linear damage accumulation law to predict creep-fatigue life for hybrid-controlled tests. The constitutive law is modified by a damage rate model linked with the dissipation of hysteresis energy through cyclic fatigue deformation and creep deformation. Several major conclusions are drawn: The constitutive law coupled with damage shows the cyclic softening behavior for both peak stress response and effective Young's modulus; the hysteresis energy related to fatigue deformation shows almost linear variation with respect to the number of cycles, while the hysteresis creep energy shows a power law increase with respect to the number of cycles; a nonlinear damage accumulation law by taking the power of the fatigue energy and creep energy fractions shows a good correlation with the final failure life. The current testing and simulation results suggest a power of ~1/3 as an estimate for the non-linear damage accumulation law. In general, the proposed methodology shows good agreement with the experimental data for hysteresis response, cyclic softening and life prediction.

6. CONCLUSION AND FUTURE WORK

The elevated temperature creep-fatigue behavior of Alloy 617 was investigated in this study, using a combination of experimental testing, image-based damage analysis, constitutive modeling and life-prediction. The initial problem of generating creep-dominated creep-fatigue interaction was resolved by selecting a non-traditional loading profile with force-controlled tensile hold periods. The failed test specimens from various tests were analyzed using Scanning Electron Microscopy (SEM), Energy Dispersive Spectroscopy (EDS), and Electron Backscatter Diffraction (EBSD). The area fraction of creep-induced voids and average length of fatigue-induced surface cracks were quantified to find correlations between creep and fatigue damage. Unlike the time fraction rule, the image based damage analysis indicated a clear trend in creep-fatigue interaction. A new life-prediction methodology based on an effective time fraction was proposed as an alternative to the traditional time fraction rule. Finally, a unified viscoplastic model with a damage variable was implemented to obtain an energy-based life prediction. The major conclusions are:

1. Strain-controlled testing is not able to generate creep-dominant CF testing results due to the rapid stress relaxation of Alloy 617 at high temperatures. On the contrary, pure force-controlled testing produces cyclic ratchetting and is therefore not ideal for the CF investigation. Hybrid controlled testing with stress hold at peak strain tends to produce very large and non-representative CF interaction due to the holding stress exceeding the initial yield stress. The proposed hybrid control loading profile with a separately controlled holding stress appears to be

well suited for the investigated material and temperature range to generate varying proportions of creep and fatigue damage.

2. Detailed imaging analysis showed that the microstructural damage features are not correlated with the classical damage diagram parameters. Specifically, the void density is not correlated with the classical time fraction. Instead, it is correlated with the time spent for the net creep strain increment. The crack length is well correlated with the cycle fraction in fatigue. Thus, the application of the classical time fraction approach is questionable for the investigated load spectrum as it is not supported by trends in physical damage.
3. An effective time fraction approach based on the image analysis shows good agreement for the life prediction under both hybrid control and strain-controlled testing. The scatter of life factor of three is observed for the in-house testing and literature experimental data. The empirical damage interaction diagram using the proposed effective time fraction approach shows a bi-linear curve for the creep and fatigue damage.
4. A unified constitutive and damage model is developed by coupling the hysteresis energy with the softening behavior of the material. The fatigue hysteresis energy and creep hysteresis energy shows monotonic relationship with respect to the Young's modulus and creep law exponent. A nonlinear power damage summation rule is proposed and shows that an exponent of ~1/3 for the two hysteresis energies. The final failure prediction is in good agreement with experiments.

Several future studies are suggested based on the current investigation

1. In-situ testing with the real time monitoring of the microstructural damage features is desired as it can provide more detailed insight of the damage progression under different loading conditions;
2. Experimental testing under a variable loading spectrums of creep-fatigue may be used to further validate the proposed methodology. It is expected that such testing is required to investigate the nonlinear interaction of creep and fatigue mechanism.
3. The current simulation study focuses on the macro level material behavior. A micromechanics-based simulation revealing failure mechanisms at the grain level is desired.
4. Uncertainties associated with the experimental testing and numerical simulation have not been addressed in the current study. Probabilistic approach is required for the failure probability and reliability estimation for future design and analysis.

7. REFERENCES

[1] K.B.S. Rodriguez, P., Rao, Nucleation and Growth of Cracks and Cavities under Creep-Fatigue Interaction, Prog. Mater. Sci. 37 (1993) 403–480.

[2] A. Dasgupta, Solder Creep-Fatigue Analysis by an Energy-Partitioning Approach, J. Electron. Packag. 114 (1992) 152–160.

[3] D. Chapin, S. Kiffer, J. Nestell, The Very High Temperature Reactor : A Technical Summary, MPR Assoc. (2004).

[4] J.M. Corum, J.J. Blass, Rules for design of Alloy 617 nuclear components to very high temperatures, Oak Ridge Natl. Lab. (1991).

[5] X. Chen, M.A. Sokolov, S. Sham, D.L. Erdman, J.T. Busby, K. Mo, J.F. Stubbins, Experimental and modeling results of creep-fatigue life of Inconel 617 and Haynes 230 at 850C, J. Nucl. Mater. 432 (2013) 94–101. doi:10.1016/j.jnucmat.2012.08.040.

[6] J.A. Simpson, J.K. Wright, L.J. Carroll, Novel Experiments to Characterize Creep-Fatigue Degradation in VHTR Alloys, Idaho Natl. Lab. (2013). http://www.osti.gov/scitech/biblio/1097150.

[7] L. Carroll, M. Carroll, Creep-Fatigue Behavior of Alloy 617 at 850 and 950°C, Idaho Natl. Lab. INL/EXT-13 (2015).

[8] L.J. Carroll, C. Cabet, M.C. Carroll, R.N. Wright, The development of microstructural damage during high temperature creep–fatigue of a nickel alloy, Int. J. Fatigue. 47 (2013) 115–125. doi:10.1016/j.ijfatigue.2012.07.016.

[9] J.K. Wright, Draft ASME Boiler and Pressure Vessel Code Section III, Division 5, Section HB, Subsection B, Code Case for Alloy 617 and Background Documentation, Idaho Natl. Lab. (2015).

[10] W.Z. Zhuang, N.S. Swansson, Thermo-Mechanical Fatigue Life Prediction: A Critical Review, 0 (1998).

[11] RCC-MRx, Design and Construction Rules for Mechanical Components of Nuclear installations, AFCEN. (2012).

[12] R.A. Ainsworth, R5 procedures for assessing structural integrity of components under creep and creep–fatigue conditions, Int. Mater. Rev. 51 (2006) 107–126. doi:10.1179/174328006X79463.

[13] Y. Takahashi, Study on creep-fatigue evaluation procedures for high-chromium steels-Part I: Test results and life prediction based on measured stress relaxation, Int. J. Press. Vessel. Pip. 85 (2008) 406–422. doi:10.1016/j.ijpvp.2007.11.008.

[14] M.W. Spindler, An improved method for calculation of creep damage during creep–fatigue cycling, Mater. Sci. Technol. 23 (2007) 1461–1470. doi:10.1179/174328407X243924.

[15] W. Hoffelner, Creep-Fatigue Life Determination of Grade 91 Steel Using a Strain-Range Separation Method, in: ASME 2009 Press. Vessel. Pip. Div. Conf., 2009: pp. 1–5. doi:10.1115/PVP2009-77705.

[16] H. Rao, K Bhanu Sankara, Meurer, H. -P, Schuster, Creep-Fatigue Interaction of lnconel 617 at 950 ° C in Simulated Nuclear Reactor Helium, Mater. Sci. Eng. A. 104 (1988) 37–51.

[17] C. Cabet, L. Carroll, R. Wright, Low Cycle Fatigue and Creep-Fatigue Behavior of Alloy 617 at High Temperature, J. Press. Vessel Technol. 135 (2013) 61401. doi:10.1115/1.4025080.

[18] H. Nickel, F. Schubert, H. Breitling, E. Bodmann, Development and qualification of materials for components for high-temperature gas-cooled reactor, Nucl. Eng. Des. (1990) 183–192. doi:10.1017/CBO9781107415324.004.

[19] B. Fournier, M. Sauzay, C. Caës, M. Noblecourt, M. Mottot, a. Bougault, V. Rabeau, a. Pineau, Creep-fatigue-oxidation interactions in a 9Cr-1Mo martensitic steel. Part I: Effect of tensile holding period on fatigue lifetime, Int. J. Fatigue. 30 (2008) 649–662. doi:10.1016/j.ijfatigue.2007.05.007.

[20] M.E. Kassner, γ/γ' Nickel-Based Superalloys, 2015. doi:10.1016/B978-0-08-099427-7.00011-6.

[21] E.P. Esztergar, Creep-fatigue Interaction and Cumulative Damage Evaluations for Type 304 Stainless Steel, Oak Ridge Natl. Lab. Rep. (1972). http://www.iaea.org/inis/collection/NCLCollectionStore/_Public/04/038/4038440.pdf.

[22] G.J. Lloyd, J. Wareing, Life prediction methods for combined creep-fatigue endurance, Met. Technol. 8 (1981) 297–305.

[23] ASME, Boiler and Pressure Vessel Code, Section III, Sub-Section NH, New York, USA, 2001.

[24] S.F. Di Martino, R.G. Faulkner, S.C. Hogg, S. Vujic, O. Tassa, Characterisation of microstructure and creep properties of alloy 617 for high-temperature applications, Mater. Sci. Eng. A. 619 (2014) 77–86. doi:10.1016/j.msea.2014.09.046.

[25] S.K. Sharma, G.D. Ko, F.X. Li, K.J. Kang, Oxidation and creep failure of alloy 617 foils at high temperature, J. Nucl. Mater. 378 (2008) 144–152. doi:10.1016/j.jnucmat.2008.04.021.

[26] T.C. Totemeier, H. Tian, Creep-fatigue–environment interactions in INCONEL 617, Mater. Sci. Eng. A. 468–470 (2007) 81–87. doi:10.1016/j.msea.2006.10.170.

[27] S. Schlegel, S. Hopkins, E. Young, J. Cole, T. Lillo, M. Frary, Precipitate Redistribution during Creep of Alloy 617, Metall. Mater. Trans. A. 40 (2009) 2812–2823. doi:10.1007/s11661-009-0027-7.

[28] F. Tahir, Y. Liu, Development of Creep-Dominant Creep-Fatigue Testing for Alloy 617, in: 57th AIAA/ASCE/AHS/ASC Struct. Struct. Dyn. Mater. Conf. San Diego, California, USA., AIAA SciTech, San Diego, 2016. doi:http://dx.doi.org/10.2514/6.2016-0668.

[29] R.N. Wright, High Temperature Materials Characterization Database, Idaho Natl. Lab. (n.d.).

[30] R. Campbell, Creep/fatigue interaction correlation for 304 stainless steel subjected to strain-controlled cycling with hold times at peak strain, J. Eng. Ind. (1971). http://manufacturingscience.asmedigitalcollection.asme.org/article.aspx?articleid=1442060.

[31] X.-L. Yan, X.-C. Zhang, S.-T. Tu, S.-L. Mannan, F.-Z. Xuan, Y.-C. Lin, Review of creep–fatigue endurance and life prediction of 316 stainless steels, Int. J. Press. Vessel. Pip. 126–127 (2015) 17–28. doi:10.1016/j.ijpvp.2014.12.002.

[32] E.L. Robinson, Effect of Temperature Variation on the Creep Strength of Steel, Trans. ASME. 60 (1938) 253–259.

[33] R.H. Priest, E.G. Ellison, A combined deformation map-ductility exhaustion approach to creep-fatigue analysis, Mater. Sci. Eng. 49 (1981) 7–17. doi:10.1016/0025-5416(81)90128-2.

[34] R. Hales, a Method of Creep Damage Summation Based on Accumulated Strain for the Assessment of Creep???Fatigue Endurance, Fatigue Fract. Eng. Mater. Struct. 6 (1983) 121–135. doi:10.1111/j.1460-2695.1983.tb00329.x.

[35] Y. Takahashi, D.G. Bilal Dogan, Systematic Evaluation of Creep-Fatigue Life Prediction Methods for Various Alloys, J. Press. Vessel Technol. 135 (2013) 61204. doi:10.1115/1.4024436.

[36] S.S. Manson, G.R. Halford, Creep-fatigue analysis by strain-range partitioning, 1971.

[37] E.H. Wong, W.D. van Driel, A. Dasgupta, M. Pecht, Creep fatigue models of solder joints: A critical review, Microelectron. Reliab. (2015). doi:10.1016/j.microrel.2016.01.013.

[38] T. Asayama, Update and Improve Subsection NH - Alternative Simplified Creep-Fatigue Design Methods, 2011.

[39] L.J. Carroll, R.N. Wright, T.-L. Sham, N.J. Lybeck, R.N. Wright, Determination of the creep-fatigue interaction diagram for Alloy 617, Proc. ASME 2016 Press. Vessel. Pip. Conf. (2016) 1–10.

[40] F. Tahir, S. Dahire, Y. Liu, Image-based Creep-Fatigue Damage Mechanism Investigation of Alloy 617 at 950°C, Mater. Sci. Eng. A. 679 (2017) 391–400. doi:10.1016/j.msea.2016.10.050.

[41] S. Taira, Lifetime of Structures Subjected to Varying Load and Temperature, in: N.J. Hoff (Ed.), Creep Struct. Colloq. Held Stanford Univ. Calif. July 11--15, 1960, Springer Berlin Heidelberg, Berlin, Heidelberg, 1962: pp. 96–124. doi:10.1007/978-3-642-86014-0_6.

[42] J.L. Chaboche, G. Rousselier, On the Plastic and Viscoplastic Constitutive Equations, Part I: Rules Developed With Internal Variable Concept, ASME J. Press. Vessel Technol. 105 (1983) 153–164.

[43] C.J. Hyde, W. Sun, T.H. Hyde, J.P. Rouse, T. Farragher, N.P. O'Dowd, S.B. Leen, Cyclic Viscoplasticity Testing and Modeling of a Service-Aged P91 Steel, J. Press. Vessel Technol. 136 (2014) 44501. doi:10.1115/1.4026865.

[44] J. Lemaitre, J.-L. Chaboche, Mechanics of Solid Materials, 1990. doi:10.1139/l92-025.

[45] J. Tong, B. Vermeulen, The description of cyclic plasticity and viscoplasticity of waspaloy using unified constitutive equations, Int. J. Fatigue. 25 (2003) 413–420. doi:10.1016/S0142-1123(02)00162-7.

[46] J. Tong, Z.L. Zhan, B. Vermeulen, Modelling of cyclic plasticity and viscoplasticity of a nickel-based alloy using Chaboche constitutive equations, Int. J. Fatigue. 26 (2004) 829–837. doi:10.1016/j.ijfatigue.2004.01.002.

[47] Z. Zhan, U.S. Fernando, J. Tong, Constitutive modelling of viscoplasticity in a nickel-based superalloy at high temperature, Int. J. Fatigue. 30 (2008) 1314–1323. doi:10.1016/j.ijfatigue.2007.06.010.

[48] J.-T. Yeom, S.J. Williams, I.-S. Kim, N.-K. Park, Unified viscoplastic models for low cycle fatique behavior of Waspaloy, Met. Mater. Int. 7 (2001) 233–240. doi:10.1007/BF03026981.

[49] M. Yaguchi, M. Yamamoto, T. Ogata, A viscoplastic constitutive model for nickel-base superalloy, part 1: Kinematic hardening rule of anisotropic dynamic recovery, Int. J. Plast. 18 (2002) 1083–1109. doi:10.1016/S0749-6419(01)00029-8.

[50] R. Ahmed, P.R. Barrett, T. Hassan, Unified viscoplasticity modeling for isothermal low-cycle fatigue and fatigue-creep stress-strain responses of Haynes 230, Int. J. Solids Struct. 89 (2015) 131–145. doi:10.1016/j.ijsolstr.2016.03.012.

[51] L. Carroll, T. Hassan, Constitutive Modeling of High Temperature Uniaxial Creep-Fatigue and Creep-Ratcheting Responses of Alloy 617, in: Proc. ASME 2013 Press. Vessel. Pip. Conf., 2013. doi:10.1115/PVP2013-97251.

[52] T.-L. Sham, K.P. Walker, Preliminary Development of a Unified Viscoplastic Constitutive Model for Alloy 617 With Special Reference to Long Term Creep Behavior, Fourth Int. Top. Meet. High Temp. React. Technol. Vol. 2. (2008) 81–89. doi:10.1115/HTR2008-58215.

[53] R. Hales, S.R. Holdsworth, M.P. O'Donnell, I.J. Perrin, R.P. Skelton, A code of practice for the determination of cyclic stress-strain data, Mater. High Temp. 19 (2002) 165–185. doi:10.3184/096034002783640332.

[54] V.G. Ramaswamy, D.C. Stouffer, J.H. Laflen, A Unified Constitutive Model for the Inelastic Uniaxial Response of Rene' 80 at Temperatures Between 538C and 982C, J. Eng. Mater. Technol. 112 (1990) 280. doi:10.1115/1.2903324.

[55] J.L. Chaboche, A review of some plasticity and viscoplasticity constitutive theories, Int. J. Plast. 24 (2008) 1642–1693. doi:10.1016/j.ijplas.2008.03.009.

[56] R. Krishna, H. V. Atkinson, S. V. Hainsworth, S.P. Gill, Gamma Prime Precipitation, Dislocation Densities, and TiN in Creep-Exposed Inconel 617 Alloy, Metall. Mater. Trans. A Phys. Metall. Mater. Sci. 47 (2015) 178–193. doi:10.1007/s11661-015-3193-9.

[57] D. Tytko, P.P. Choi, J. Kl??wer, A. Kostka, G. Inden, D. Raabe, Microstructural evolution of a Ni-based superalloy (617B) at 700°C studied by electron microscopy and atom probe tomography, Acta Mater. 60 (2012) 1731–1740. doi:10.1016/j.actamat.2011.11.020.

[58] X. Chen, Z. Yang, M. a. Sokolov, D.L. Erdman, K. Mo, J.F. Stubbins, Effect of creep and oxidation on reduced fatigue life of Ni-based alloy 617 at 850°C, J. Nucl. Mater. 444 (2014) 393–403. doi:10.1016/j.jnucmat.2013.09.030.

[59] F.P.E. Dunne, D.R. Hayhurst, Continuum damage based constitutive equations for copper under high temperature creep and cyclic plasticity, Proc. R. Soc. A. 437 (1992) 545–566. doi:10.1098/rspa.1983.0054.

[60] W. Wang, P. Buhl, A. Klenk, Y. Liu, A Continuum Damage Mechanics-Based Viscoplastic Model of Adapted Complexity for High-Temperature Creep–Fatigue Loading, J. Eng. Gas Turbines Power. 138 (2016) 92501. doi:10.1115/1.4032679.

[61] T.W. Kim, D.H. Kang, J.T. Yeom, N.K. Park, Continuum damage mechanics-based creep-fatigue-interacted life prediction of nickel-based superalloy at high temperature, Scr. Mater. 57 (2007) 1149–1152. doi:10.1016/j.scriptamat.2007.08.014.

[62] J.L. Chaboche, G. Rousselier, On the Plastic and Viscoplastic Constitutive Equations - Part II: Applications of Internal Variable Concepts to the 316 Stainless Steel, J. Press. Vessel Technol. 105 (1983) 159–164.

[63] C.O. Frederick, P.J. Armstrong, A mathematical representation of the multiaxial

Bauschinger effect, Mater. High Temp. 24 (2007) 1–26. doi:10.1179/096034007X207589.

[64] Y.P. Gong, C.J. Hyde, W. Sun, T.H. Hyde, Determination of material properties in the Chaboche unified viscoplasticity model, Proc. Inst. Mech. Eng. Part L J. Mater. Des. Appl. 224 (2009) 19–29. doi:10.1243/14644207JMDA273.